

Strong Hilbert space fragmentation via emergent quantum drums in two dimensions

Anwasha Chattopadhyay^{1,2}, Bhaskar Mukherjee³, K. Sengupta¹, Arnab Sen^{1*}

¹ School of Physical Sciences, Indian Association for the Cultivation of Science, Jadavpur, Kolkata 700032, India.

² Department of Physics, School of Mathematical Sciences, Ramakrishna Mission Vivekananda Educational and Research Institute, Belur, Howrah 711202, India.

³ Department of Physics and Astronomy, University College London, Gower Street, London WC1E 6BT, United Kingdom

* tpars@iacs.res.in

August 31, 2022

Abstract

We introduce a disorder-free model of $S = 1/2$ spins on the square lattice in a constrained Hilbert space where two up-spins are not allowed simultaneously on any two neighboring sites of the lattice. The interactions are given by ring-exchange terms on elementary plaquettes that conserve both the total magnetization as well as dipole moment. We show that this model provides a tractable example of strong Hilbert space fragmentation in two dimensions with typical product states in the computational basis evading thermalization. Given any product state, the system can be decomposed into disjoint spatial regions made of edge and/or vertex sharing plaquettes that we dub as “quantum drums”. These quantum drums come in many shapes and sizes and specifying the plaquettes that belong to a drum fixes its spectrum. The spectra of some small drums is calculated analytically. We study two bigger quasi-one-dimensional drums numerically, dubbed “wire” and a “junction of two wires” respectively. We find that these possess a chaotic spectrum but also support distinct families of quantum many-body scars that cause periodic revivals from different initial states. The wire is shown to be equivalent to the one-dimensional PXP chain with open boundaries, a paradigmatic model for quantum many-body scarring, while the junction of two wires represents a distinct constrained model.

Contents

1	Introduction	2
2	Model and its properties	5
2.1	Quantum drums	7
2.1.1	Constructing drums from a product state	8
2.1.2	Shielding region and closest approach of drums	10
2.1.3	Recursive construction of drums	11
2.1.4	Wires, junctions of wires, other quasi-1D and 2D drums	13

2.2	Exact diagonalization of small lattices and deciphering spectrum using drums	15
2.3	Eigenstates with integer energies from packing of one-plaquette drums	17
3	Strong Hilbert space fragmentation	19
3.1	Numerical evidence from exact diagonalization	19
3.2	Wire decomposition of quantum drums	20
3.3	Absence of thermalization from typical product states	25
4	Analytical study of small quantum drums	31
4.1	Tree structure	32
4.2	Wire	32
4.3	Junction units	33
5	Numerical study of large quantum drums	36
5.1	Tree generating algorithm and equivalence of wire to 1D PXP chain	36
5.2	Hilbert space dimension and level statistics	39
5.3	Zero modes and index theorem	41
5.4	QMBS and related diagnostics	42
6	Discussion	48
	References	49

1 Introduction

A generic isolated quantum system with many degrees of freedom is expected to “self-thermalize” as it evolves unitarily under the dynamics of its own Hamiltonian [1]. This implies that pure states obtained from the time evolution of different initial states that share the same energy density cannot be distinguished from each other at late times using only local probes. A microscopic justification for this self-thermalization is provided by the eigenstate thermalization hypothesis (ETH) [2–5] that posits that high-energy eigenstates of such systems appear locally thermal with the temperature being set by the energy density of the eigenstate.

Rapid progress in producing and manipulating well-isolated quantum simulators such as ultracold gases [6, 7], trapped ions [8], Rydberg atom arrays [9] and superconducting qubits [10] has made it possible to study thermalization and its violations in such platforms. In particular, the experimental observation of late-time coherent oscillations from certain simple high-energy initial states in a kinetically-constrained chain of 51 Rydberg atoms [11] generated great interest in understanding thermalization in interacting theories with constrained Hilbert spaces. The revivals reported in Ref. [11] were shown to arise due to the large overlap of some simple initial states with a small set of nonthermal high-energy eigenstates, dubbed quantum many-body scars (QMBS) in Refs. [12, 13], in an otherwise non-integrable PXP model [14, 15] that served as the minimal model for the experiment.

Subsequent theoretical studies have shown a plethora of interesting non-ergodic behavior in various models with constrained Hilbert spaces, including Hamiltonian formulations of lattice

gauge theories [16–20] that may be realizable on quantum simulators [21–23]. These include different varieties of QMBS [24–45], disorder-free localization [46–49] as well as a richer ergodicity-breaking paradigm dubbed Hilbert space fragmentation [50, 51]. Such forms of ETH-violation are distinct from the breakdown of ETH due to many-body localization [52–54] where strong disorder plays a crucial role.

Systems with Hilbert space fragmentation [55–68] often feature multiple conservation laws [50, 51] which severely restrict the mobility of excitations. In such cases, the Hilbert space can split into exponentially many dynamically disconnected *fragments*. These fragments cannot be distinguished by any obvious global symmetries of the Hamiltonian [50, 51]. Such fragments can either be finite or infinite-dimensional matrices in the thermodynamic limit and can show vastly different dynamical properties, such as integrability [57, 65], disorder-free localization [46–49, 56, 60] or QMBS [64, 66] though large fragments are expected to typically satisfy a Krylov-restricted version of ETH [55]. Both *weak* and *strong fragmentation* is known to exist in one-dimensional (1D) models [50, 51], with the two cases distinguished by whether the fraction of eigenstates violating the ETH are a set of measure zero or not in the thermodynamic limit. Weakly fragmented systems are similar to systems with QMBS since both situations lead to weak ergodicity breaking where typical initial states still thermalize [69]. However, strongly fragmented systems present a distinct form of ergodicity breaking that is different from systems with QMBS.

In Ref. [50], 1D spin models with both global charge and dipole conservation laws were considered and it was argued that such dipole-conserving models should exhibit Hilbert space fragmentation in any dimension [50, 51] (for examples of fragmentation without global dipole conservation, see Refs. [31, 57, 58, 60, 62, 64, 66, 67]). One of the tell-tale signs of fragmentation in such models is an exponential number of completely inert states that form 1×1 fragments on their own. While examples of both weak and strong fragmentation are known in one dimension, it is not clear whether global dipole conservation alone is sufficient to lead to strong fragmentation in higher dimensions. This extra conservation ensures that Hilbert space fragments of different sizes can be constructed by embedding suitable “active” regions into “inert” backgrounds and surrounding the “active” regions by “shielding” regions; the shielding region, however, turns out to be of the same size or bigger than the active region it isolates [51]. This makes it difficult to construct explicit examples of strong fragmentation in two or higher dimensions.

In this paper, we will construct a model that shows strong Hilbert space fragmentation in two dimensions by considering $S = 1/2$ spins (equivalently, hard-core bosons) on the square lattice with ring-exchange terms on elementary plaquettes that are consistent with total magnetization (equivalently, boson number) conservation as well as global dipole moment conservation. The important additional ingredient in the model is the presence of a kinematic constraint that no two nearest neighbor sites can have two up-spins (bosons) simultaneously. Similar models with ring-exchange and other competing terms, but without the additional hard-core constraints, are known to have interesting low-energy phases and transitions [70–72]. High-energy properties of the unconstrained model with only the ring-exchange terms were studied recently in Ref. [68] where it was realized that such terms imply subsystem symmetries associated with the conservation of magnetization along each column and row of the square lattice. This leads to global dipole conservation and consequently Hilbert space fragmentation. However, as we will show here, the enforcement of the kinematic constraints leads to several additional features, including strong ergodicity breaking and the emergence of “quantum drums”, that were absent in the model considered in Ref. [68]. The quantum drums here can be viewed as the “active” regions which can then be surrounded by “shielding” regions of $O(1)$ thickness (in lattice units). Crucially, the thickness of the shielding regions does not grow with the size of the quantum drums. Each quantum

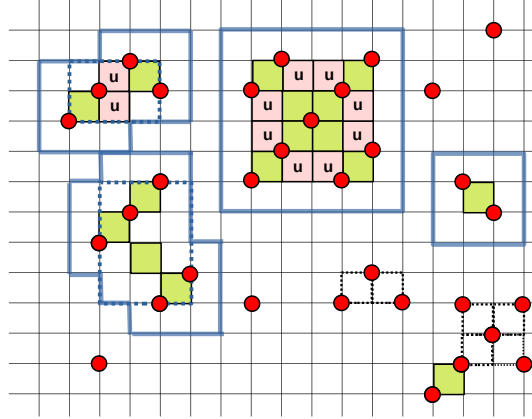


Figure 1: An initial state on the square lattice where the up-spins (bosons) are indicated in red while the other sites have down-spins (no bosons). The five quantum drums that correspond to this initial state are shown with their elementary plaquettes shaded. Plaquettes that are colored as green can have two up-spins (bosons) along both its two diagonals during quantum evolution as explained in the text. The pink plaquettes, also labeled by “u”, can have two up-spins (bosons) only along one of its two diagonals. Sites that do not belong to any of these five drums have inert up/down spins fixed by the initial condition. Each drum generates a separate fragment in Hilbert space with the corresponding fragment dimension being 3×3 for the top-left drum, 7×7 for the bottom-left drum, 24×24 for the middle drum and 2×2 for both the top-right and bottom-right drums. The shielding regions of the drums are shown using thick blue lines.

drum is made of edge and/or vertex sharing elementary plaquettes and specifying the plaquettes that make a drum uniquely fixes its spectrum, thus justifying this particular nomenclature. We refer the reader to Fig. 1 for an example of quantum drums and their corresponding shielding regions that emerge from a particular initial state.

All the Hilbert space fragments of this model that are not 1×1 , i.e., that do not correspond to inert Fock states, can be generated from a combination of appropriate quantum drums embedded in an otherwise inert background (which may itself shrink to zero for certain drums) (see Fig. 1). These quantum drums come in a variety of shapes and sizes and can be made of a finite number or an arbitrarily large number of plaquettes in the thermodynamic limit. Crucially, the scaling of the size of the Hilbert space fragments generated from large drums allows for a proof of lack of thermalization for any typical Fock state by identifying either (a) an extensive number of single spin correlators or (b) an extensive number of next-nearest neighbor two-spin correlators whose expectation values stay pinned to their initial (non-thermal) values. To the best of our knowledge, this interacting theory provides the first example of *strong* Hilbert space fragmentation in two dimensions.

The rest of the paper is arranged as follows. In Sec. 2, we introduce the model and summarize some of its important properties. In Sec. 2.1, we discuss the quantum drums that emerge in this model in more details. The classical construction of the drums, given an initial state, is explained in Sec. 2.1.1. The construction of the shielding regions of drums and closest approach of two drums such that these can still be considered independent of each other is explained in Sec. 2.1.2. In Sec. 2.1.3, a recursive procedure to generate bigger quantum drums starting from the most

elementary one-plaquette drum is detailed. We introduce some particular drums, dubbed wires and different junctions of wires and some other quasi-one dimensional (1D) and two-dimensional (2D) drums in Sec. 2.1.4. In Sec. 2.2, we give numerical evidence that the energy eigenvalues and their associated degeneracies from exact diagonalization (ED) on small systems can be completely understood in terms of the spectra of the quantum drums. We construct a large class of eigenstates with integer eigenvalues (including zero modes) from the packing of the simplest one-plaquette quantum drums in Sec. 2.3. Evidence for strong Hilbert space fragmentation for this model is presented in Sec. 3. The numerical evidence from ED is presented in Sec. 3.1. A wire decomposition of drums is introduced in Sec. 3.2 which allows us to derive the scaling of the dimension of the Hilbert space fragments associated with large 2D drums and also determine which kinds of drums dominate statistically given a certain density of up-spins (bosons) in Sec. 3.3. This insight leads to the proof that typical initial product states *do not* thermalize in Sec. 3.3 by identifying either an extensive number of single-spin correlators or two-spin correlators that stay pinned to their initial non-thermal values. The analytical study for the spectra of certain small quantum drums is given in Sec. 4. A tree structure to represent the action of H in the Fock space of a drum is explained in Sec. 4.1. The spectra of small wires is calculated in Sec. 4.2 while the spectra of other small quantum drums that can be viewed as building blocks of more complicated wire junctions is calculated in Sec. 4.3. The spectra of two different classes of bigger quasi-1D quantum drums, a wire and a particular junction of two wires, are addressed numerically using exact diagonalization (ED) in Sec. 5. Both these large quantum drums can be interpreted as effective quasi-1D models with a spectrum that is symmetric around zero energy. A tree generating algorithm is described and the equivalence of the wire to the 1D PXP model on an open chain is shown in Sec. 5.1. The Hilbert space dimensions for both the drums are calculated analytically and level statistics are computed numerically in Sec. 5.2. The Hilbert space structure of the junction of two wires turns out to be completely different from that of the wire as discussed in both Sec. 5.1 and Sec. 5.2. One of these fragments is shown to have a macroscopically large number of exact zero modes while the other fragment has no zero modes in Sec. 5.3. Both fragments satisfy Krylov-restricted ETH but also support distinct families of QMBS that result in periodic revivals from different simple initial states as discussed in Sec. 5.4. Our numerical results for the wire show that open PXP chains of length $3n + 1$, where n is an integer, lead to enhanced fidelity revivals for the period-3 ordered initial $|\mathbb{Z}_3\rangle$ state without adding any optimal perturbations to the bare Hamiltonian; a feature which may have experimental consequence for Rydberg chains. The junction of two wires also shows QMBS and simple initial states from which clear revivals in fidelity are observed. Finally, we summarize our main results and conclude in Sec. 6.

2 Model and its properties

The Hamiltonian of the model is given by

$$H = J \sum_{j_x, j_y} \left(\sigma_{j_x, j_y}^+ \sigma_{j_x+1, j_y+1}^+ \sigma_{j_x+1, j_y}^- \sigma_{j_x, j_y+1}^- + \text{h.c.} \right) \quad (1)$$

where σ_{j_x, j_y}^α for $\alpha = x, y, z$ represent spin-half Pauli matrices at sites (j_x, j_y) of a 2D square lattice, $\sigma_{j_x, j_y}^\pm = (\sigma_{j_x, j_y}^x \pm i\sigma_{j_x, j_y}^y)/2$, and the lattice spacing has been set to unity. The Hamiltonian is supplemented by the constraint that two up-spins can not occupy neighboring sites of the lattice;

this is implemented by the operator relation

$$\left(1 + \sigma_{j_x, j_y}^z\right) \left(1 + \sigma_{j_x \pm 1, j_y}^z\right) = \left(1 + \sigma_{j_x, j_y}^z\right) \left(1 + \sigma_{j_x, j_y \pm 1}^z\right) = 0 \quad (2)$$

For finite $L_x \times L_y$ rectangular lattices, we will consider open boundary conditions and the constraint (Eq. 2) is then applied to the three/two nearest neighbors of (j_x, j_y) for the edge/corner sites.

This system maps exactly to hard-core bosons with the following transformations:

$$\begin{aligned} 2b_{j_x, j_y}^\dagger b_{j_x, j_y} - 1 &= \sigma_{j_x, j_y}^z \\ b_{j_x, j_y}^\dagger &= \sigma_{j_x, j_y}^+ \end{aligned} \quad (3)$$

where b_{j_x, j_y}^\dagger is the boson creation operator and $n_{j_x, j_y} = b_{j_x, j_y}^\dagger b_{j_x, j_y}$ is the boson number operator at site (j_x, j_y) . For the rest of this work, we shall set $J = 1$. The terms in Eq. 1 can be viewed as ring-exchange terms on elementary plaquettes which convert a clockwise arrangement of σ^z from being $(+1, -1, +1, -1)$ to $(-1, +1, -1, +1)$ (equivalently, an arrangement of bosons from $(1, 0, 1, 0)$ to $(0, 1, 0, 1)$) and vice-versa and annihilate other arrangements on a plaquette. It is convenient to define a vacuum state where all sites of the lattice have down-spins, i.e., no bosons for future reference. This model has the following properties:

- The many-body spectrum of H is symmetric around the energy $E = 0$ for any finite $L_x \times L_y$ lattice with open boundary conditions (OBC). This is because the operator defined by

$$\mathcal{C} = \prod_{(j_x, j_y) \in (\text{even}, \text{even})} \sigma_{j_x, j_y}^z \quad (4)$$

satisfies $\{H, \mathcal{C}\} = 0$ where $\prod_{(j_x, j_y) \in (\text{even}, \text{even})}$ denotes a product over all the sites (j_x, j_y) of the lattice such that both j_x, j_y are even. This implies that any many-body eigenstate of H with an energy E and denoted by $|E\rangle$ has a partner $\mathcal{C}|E\rangle$ that has the energy $-E$.

- Apart from discrete symmetries like rotations by $\pi/2$ (for $L_x = L_y$ lattices) and π (for $L_x \neq L_y$ lattices), the model has a discrete reflection symmetry \mathcal{R} where the axis of reflection can be taken to be the diagonal through $(0, 0)$ for $L_x = L_y$ or the perpendicular bisector of the longer side when $L_x \neq L_y$. \mathcal{R} commutes both with the Hamiltonian H and the ‘‘chirality’’ operator \mathcal{C} . This has the important consequence that the spectrum has exact zero modes whose number scales exponentially with the system size due to an index theorem shown in Ref. [73]. These zero modes are the only eigenstates of H that also possess a definite ‘‘chiral charge’’ of ± 1 under the action of \mathcal{C} .
- The model conserves the total magnetization (boson number) defined by $S_{\text{tot}}^z = \sum_{j_x, j_y} \sigma_{j_x, j_y}^z$. More interestingly, it conserves the following dipole moments in the x and y directions:

$$D_x = \sum_{j_x, j_y} j_x \sigma_{j_x, j_y}^z, \quad D_y = \sum_{j_x, j_y} j_y \sigma_{j_x, j_y}^z. \quad (5)$$

This property follows from the fact that the total magnetization on each column and each row of the square lattice is separately conserved under the dynamics induced by H (Eq. 1) as pointed out earlier in Ref. [68] in a similar model, but without the Hilbert space constraints. Models with the simultaneous conservation of total charge and dipole moment have been shown to have the property of Hilbert space fragmentation [50, 51]. This model is also fragmented due to the same reasons.

- The simultaneous conservation of magnetization on each column and each row of the $L_x \times L_y$ lattice also implies disorder-free localization for a large class of initial states. To see this, let us consider the vacuum state on a $L_x \times L_y$ lattice with OBC and then create an excitation by flipping a subset of spins to $\sigma_j^z = +1$ such that the sites labelled by j are contained inside or on the boundaries of a rectangle of finite extent smaller than the entire lattice. The aforementioned conservation property then ensures that these $\sigma^z = +1$ spins cannot be transported outside this bounding rectangle since all the rows/columns outside this region have their magnetizations pinned to their lowest possible value.
- This model has an exponentially large number (in system size) of zero modes that are simply inert states, i.e., Fock states in the computational basis that are annihilated by all the local terms in H , a property shared by other models that simultaneously conserve total charge and dipole moment. However, the constrained nature of the Hilbert space also leads to an exponentially large number of *non-trivial* zero modes that emerge from Hilbert space fragments of various dimensions larger than 1×1 , ranging from 3×3 to $c^{L_x L_y} \times c^{L_x L_y}$ fragments, with $c > 1$, for $L_x, L_y \gg 1$.
- This model possesses exact non-zero integer eigenstates whose number also scales exponentially in $L_x L_y$ for integer eigenvalues ranging from ± 1 to $\pm O(\sqrt{L_x L_y})$ for $L_x, L_y \gg 1$.

2.1 Quantum drums

Due to the structure of H (Eq. 1) and the nature of the constrained Hilbert space (Eq. 2), elementary plaquettes can have a maximum of two up-spins (bosons), along any one of the two diagonals, and these are the only local configurations that can have any dynamics. Furthermore, a plaquette with two up-spins (bosons) can influence the number of possible local configurations in neighboring two-spin plaquettes even if it can have the two up-spins (bosons) only along one of the diagonals but not the other due to kinematic constraints (Eq. 2). These two facts lead to the emergence of dynamically disconnected spatial structures called quantum drums on a $L_x \times L_y$ lattice with OBC.

To understand these drums, let us imagine a *classical* Markov process in which the *transition* from one Fock state to another is caused by a ring-exchange on some elementary plaquette with two up-spins (bosons). In the presence of the hard-core constraints specified in Eq. 2, the configuration space splits into mutually inaccessible fragments, with all configurations within a fragment being mutually accessible via some finite sequence of the allowed transitions. Crucially, each such fragment can be associated to a unique real-space structure composed of a collection of connected elementary plaquettes that share edges and/or vertices. The Hamiltonian H (Eq. 1) acts in the space of mutually accessible configurations of each such fragment to generate the spectra of these quantum drums. From a dynamical point of view, the precise nature of the quantum drums is imprinted in the particular initial state that the system starts from.

We will specify two complementary construction procedures for quantum drums below, one which starts from a given product state in the computational basis (Sec. 2.1.1) and the other where the drums are constructed recursively starting from the most elementary one-plaquette drum (Sec. 2.1.3). Some of the important properties of quantum drums, which will be detailed out in the rest of the paper, are summarized below:

- Quantum drums are constructed of connected elementary plaquettes that share edges/vertices. A drum has no site that contains an inert up-spin (boson).

- All many-body eigenstates of H (Eq. 1) can be expressed in terms of the tensor product of eigenstates of appropriate quantum drums and of the remaining inert (up/down) spins (if any) on sites that do not belong to any quantum drum. This point is illustrated in detail using ED results in Sec. 2.2.
- The spectrum of a drum is uniquely fixed once the plaquettes that belongs to it are specified. The spectrum of any quantum drum is symmetric around $E = 0$. This follows from the above mentioned point and implies the existence of a corresponding chiral operator $\mathcal{C}_{\text{drum}}$ for each such drum.
- A class of quasi-1D and 2D quantum drums have an internal reflection symmetry $\mathcal{R}_{\text{drum}}$ that commutes with $\mathcal{C}_{\text{drum}}$ resulting in an exponential number of exact zero modes as the size of the drum is increased.
- Any quantum drum conserves the total magnetization when only the spins (bosons) on the sites that belong to the drum are considered.
- Any quantum drum satisfies an internal subsystem symmetry of simultaneous conservation of magnetizations along each column and each row (where the column and row is defined with respect to the background $L_x \times L_y$ lattice) of the drum.

2.1.1 Constructing drums from a product state

We first give a construction procedure that fixes all the quantum drums given a classical Fock state on a $L_x \times L_y$ lattice with OBC. An initial Fock state and its associated drums are shown in Fig. 1. The construction procedure is schematically shown in Fig. 2 for two drums starting from different Fock states. Given the Fock state, firstly all plaquettes with two up-spins (bosons) are shaded. Ring-exchange moves are attempted on such plaquettes to see whether any additional plaquettes with two up-spins (bosons) are generated which are again shaded. This process is repeated with the newly shaded plaquettes until no additional shaded plaquettes are generated. The shaded plaquettes are then subdivided into connected regions that comprise of elementary plaquettes that share edges and/or vertices. A final check has to be performed on each of these connected regions separately to construct the quantum drums. If the mutually accessible Fock states from a connected region have certain sites where any up-spin (boson) remains the same in each of the configurations, these up-spins (bosons) are then labelled as inert and the shaded plaquettes containing any inert up-spins (bosons) are unshaded. The remaining shaded plaquettes that are still connected to each other via an edge or a vertex forms a quantum drum. This last check is necessary to rule out inert structures made entirely of plaquettes with two up-spins (bosons) [see Fig. 1 for an example composed of three up-spins (bosons) on two edge-sharing plaquettes] and to find spatial structures that can be decomposed into an inert region of up-spins (bosons) and a smaller quantum drum [see Fig. 1, bottom right for an example of such a decomposition].

Two simple examples of this construction are given for initial classical Fock states on a 7×7 lattice in Fig. 2 (top-left and middle-left panels), where the filled circles indicate up-spins (bosons) while the other sites have down-spins (no bosons). Let us first consider the top three panels. The initial state is given in the top-left panel marked as A and three plaquettes are shaded at this stage. Implementing ring-exchange moves on two of the shaded plaquettes indicated by crosses in the top-left panel generates two more shaded plaquettes as shown in top-middle panel. Implementing ring-exchange moves on the shaded plaquettes indicated by crosses in that panel generates another shaded plaquette in the top-right panel and further ring-exchanges do not generate any additional

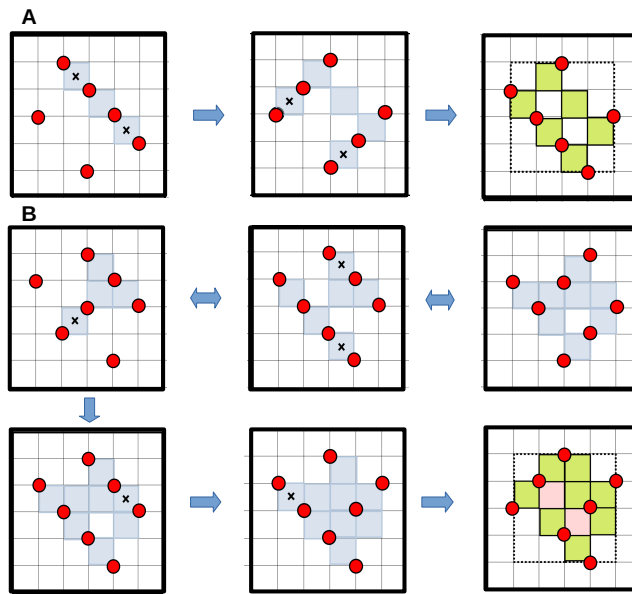


Figure 2: Illustration of the recursive construction of a quantum drum given two different initial states (marked by A and B in the figure) on a 7×7 lattice with OBC where the filled red dots indicate up-spins. The shaded plaquettes form part of a drum with the top-right and bottom-right panels indicating the drums for the initial states marked A and B respectively. A cross at the center of a plaquette indicates that a ring-exchange move is carried out for that plaquette. The green (pink) plaquettes in the top-right and bottom-right panels follow the same convention as used in Fig. 1.

shaded plaquettes. The quantum drum generated by this initial state only contains elementary plaquettes that share vertices.

The initial state in the middle-left panel marked by B gives four shaded plaquettes. Implementing ring-exchange to this state for the plaquette indicated by a cross generates two more shaded plaquettes as shown in the following panel to the right. Carrying out ring-exchange moves on two more plaquettes as indicated by crosses generates two additional shaded plaquettes. To generate the other two shaded plaquettes that form the entire quantum drum, we go back to the initial Fock state shown in the bottom-left panel and perform two ring exchange moves on the plaquettes indicated by a cross one after the other as indicated in the bottom panels. The resulting quantum drum consists of only edge-sharing plaquettes in this case.

Both the quantum drums shown in Fig. 2 generate 11×11 dimensional Hilbert space fragments respectively, diagonalizing which results in the following eigenvalues:

$$\begin{pmatrix} \pm \sqrt{\frac{1}{2}(9 \pm \sqrt{57})}, \pm \sqrt{3}, \pm \sqrt{2}, 0, 0, 0 \\ (\pm 2\sqrt{2}, \pm \sqrt{3}, -1, -1, +1, +1, 0, 0, 0) \end{pmatrix} \quad (6)$$

where the top (bottom) line in Eq. 6 refers to the eigenvalues for the quantum drum shown in the top-right (bottom-right) panel of Fig. 2. These two examples already illustrate that drums can have non-trivial zero modes, nonzero integer-valued eigenstates as well as eigenstates with irrational eigenvalues. We refer the reader to Sec. 4 for the explicit construction of the Hilbert space fragments associated to some small quantum drums.

2.1.2 Shielding region and closest approach of drums

Each quantum drum is associated with a shielding region of its own such that two quantum drums can fluctuate independently as long as the boundaries of their corresponding shielding regions do not cross. Given any Fock state consistent with a single quantum drum composed of a finite number of elementary plaquettes with the rest of the sites that do not belong to the drum being $\sigma^z = -1$ (no bosons), the corresponding shielding region can again be fixed by a classical construction. The shielding region only consists of a subset of the elementary plaquettes that directly share edges/vertices with the plaquettes on the perimeter of a quantum drum, irrespective of the size of the drum. Thus, the thickness of the shielding region *does not* scale with the size of the quantum drum and remains $O(1)$ in lattice units (e.g., see Fig. 1 and Fig. 3).

Let us first consider an elementary one-plaquette quantum drum starting from the vacuum state and then placing two $\sigma^z = +1$ spins (bosons) along any one of the diagonals of an elementary plaquette. Given this Fock state, ring-exchange is possible on only this elementary plaquette which then generates another Fock state where the $\sigma_z = +1$ spins (bosons) get transported to the other diagonal of this plaquette. Considering both these Fock states to compute

$$n_{\square_j} = \max(2 + (\sigma_{j_x, j_y}^z + \sigma_{j_x+1, j_y}^z + \sigma_{j_x, j_y+1}^z + \sigma_{j_x+1, j_y+1}^z)/2) \quad (7)$$

on each plaquette of the lattice, we see that $n_{\square_j} = 2$ for the flippable plaquette which is surrounded by $n_{\square_j} = 1$ and $n_{\square_j} = 0$ plaquettes, respectively (Fig. 3, left panel). The $n_{\square_j} = 2$ plaquette defines the quantum drum while the $n_{\square_j} = 1$ plaquettes along the perimeter of the quantum drum define the shielding region associated with this drum. The shielding region terminates at the boundary of these $n_{\square_j} = 1$ and the $n_{\square_j} = 0$ plaquettes (Fig. 3, left panel). By construction, the sites at

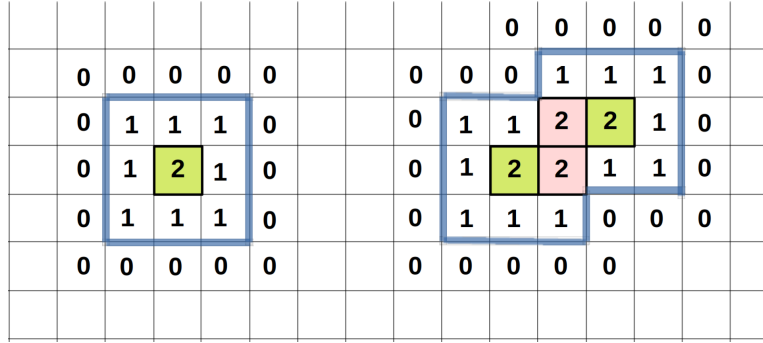


Figure 3: Two quantum drums are shown in the left and the right panels. The integers shown inside each plaquette refers to n_{\square_j} given by Eq. 7 on each plaquette of the lattice using all the Fock states generated when the quantum drum is embedded in the vacuum state. The green (pink) plaquettes in the two quantum drums follow the same convention as used in Fig. 1. The shielding regions of both drums are shown using thick blue lines and mark the boundary between the $n_{\square_j} = 1$ and the $n_{\square_j} = 0$ plaquettes.

the boundary of the shielding region cannot have $\sigma^z = +1$ spins (bosons). A more complicated quantum drum is shown in Fig. 3, right panel which can be generated from the vacuum state by, e.g., placing two $\sigma^z = +1$ spins (bosons) each along parallel diagonals of the left-most and the right-most plaquette contained in the quantum drum such that the hard-core constraints are not violated. Performing all possible ring-exchanges for this quantum drum generates two more Fock states. Considering these three Fock states to compute n_{\square_j} on each plaquette of the lattice, the four $n_{\square_j} = 2$ plaquettes, which are all connected to each other by edges for this particular drum, now define this bigger quantum drum (Fig. 3, right panel) while the $n_{\square_j} = 1$ plaquettes along the perimeter of the quantum drum define the shielding region as before (Fig. 3, right panel). The shielding region is more complicated compared to the one-plaquette drum and its boundary is again defined by the boundary of the $n_{\square_j} = 1$ and the $n_{\square_j} = 0$ plaquettes (Fig. 3, right panel). This classical construction procedure for the shielding region can be carried out for any arbitrary quantum drum composed of a finite number of elementary plaquettes.

We can now ask for the closest approach of any two quantum drums such that both the drums can be viewed to be independent of each other. The answer is that the boundaries of their corresponding shielding regions, which do not carry $\sigma^z = +1$ spins (bosons), cannot penetrate each other but can at most touch each other. For example, this is the case in the example considered in Fig. 1 which explains why the different quantum drums can be considered to be independent of each other. If the boundaries cross each other, the shielding regions have to necessarily change which also changes the corresponding quantum drums in their interior according to one of the following three possibilities: (i) the two quantum drums fuse to produce a bigger quantum drum, (ii) a spatial structure is produced such that it can be decomposed into an inert region of up-spins (bosons) and a smaller quantum drum, and (iii) a fully inert region of up-spins (bosons) is formed.

2.1.3 Recursive construction of drums

We now present a complementary drum construction procedure to the one explained in Sec. 2.1.1 which does not need the specification of a product state on the entire $L_x \times L_y$ lattice. Instead, this

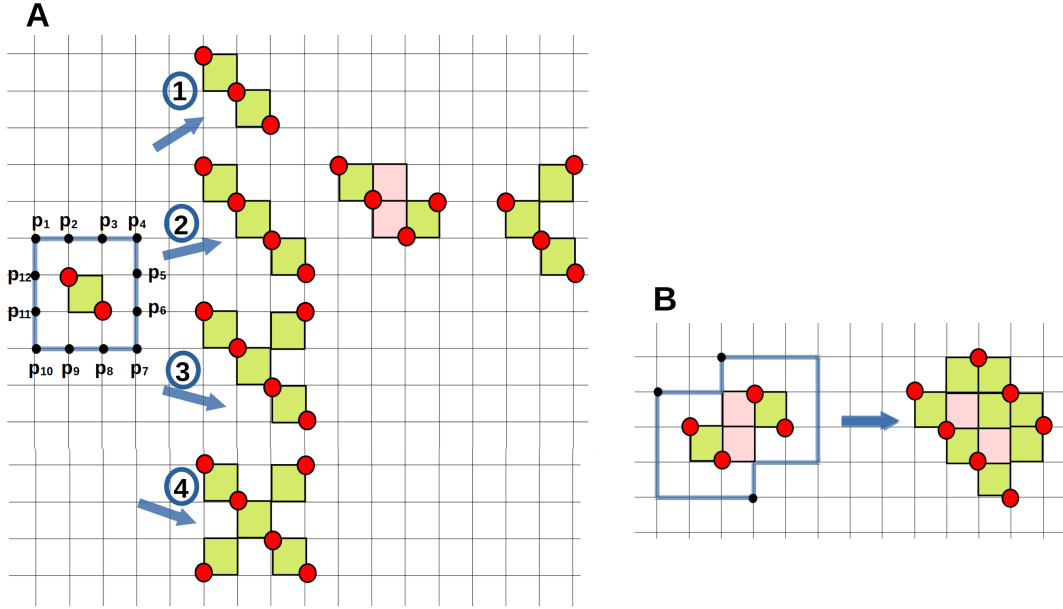


Figure 4: The left panel shows how adding up-spins (bosons) to the sites at the boundary of the shielding region (indicated by thick blue lines and also labelled from p_1 to p_{12}) of an elementary one-plaquette drum (marked as A) leads to a variety of larger quantum drums which are grouped according to the addition of \textcircled{n} up-spins (bosons) where $n = 1, 2, 3, 4$. The right panel illustrates the same concept for a more complicated quantum drum (marked as B) where three up-spins (bosons) (indicated by black dots) are added to three sites of the boundary of the shielding region (indicated by thick blue lines). Filled red dots indicate up-spins (bosons). The green (pink) plaquettes in all the quantum drums follow the same convention as used in Fig. 1.

recursive construction creates larger drums starting from smaller ones. We start with a Fock state consistent with a particular quantum drum composed of certain connected plaquettes, where the sites that do not belong to the drum are assigned $\sigma^z = -1$ spins (no bosons). This is equivalent to embedding the quantum drum in the vacuum state. By definition, the boundary of the shielding region of such a drum has $\sigma^z = -1$ (no bosons). A natural way to construct bigger drums is to choose a subset of the sites that belong to this boundary of the shielding region and then replace $\sigma^z = -1$ by $\sigma^z = +1$ at these selected sites. This generates a new Fock state from which, using the procedure of identifying a drum from a Fock state explained in Sec. 2.1.1, one gets one of the following three possibilities: (i) a bigger quantum drum with no inert up-spins (bosons), (ii) a partially active structure that can be decomposed into a smaller quantum drum and a non-zero number of inert up-spins (bosons), and (iii) a completely frozen structure with all up-spins (bosons) being inert.

Two examples of this recursive construction to generate bigger drums starting from a smaller drum are shown in Fig. 4. We first start with a Fock state consistent with an elementary one-plaquette drum in the left panel of Fig. 4, marked as A. In this case, the boundary of the shielding region is a square that consists of twelve sites, labelled as p_1, \dots, p_{12} in Fig. 4. New Fock states, consistent with larger drums, can be created by adding one/two/three or four up-spins (bosons) in this boundary region as indicated by the groups labelled by $\textcircled{1}$, $\textcircled{2}$, $\textcircled{3}$ and $\textcircled{4}$ in Fig. 4, left panel.

Adding a single up-spin (boson) at p_1 or p_4 generates Fock states consistent with a drum composed of two elementary plaquettes that share a vertex as shown in Fig. 4, left panel, group labelled by ①. Adding two up-spins (bosons) on the boundary of the shielding region in different ways leads to Fock states consistent with three different drums as shown in Fig. 4, left panel, group labelled by ②. E.g., adding up-spins (bosons) at p_1 and p_7 leads to a Fock state consistent with a drum with three plaquettes that share vertices along a single diagonal (leftmost drum shown in the group labelled by ② in left panel of Fig. 4), at p_1 and p_5 leads to a Fock state consistent with a drum with four plaquettes that are connected by edges (middle drum shown in the group labelled by ② in left panel of Fig. 4), and at p_4 and p_7 leads to a Fock state consistent with a drum with three plaquettes that again share vertices, but not along a single diagonal (rightmost drum shown in the group labelled by ② in left panel of Fig. 4)). Adding three up-spins (bosons) at, e.g., p_1 , p_4 and p_7 , leads to a Fock state consistent with a quantum drum with four plaquettes that are connected by vertices as shown in the group labelled by ③ in left panel of Fig. 4. Finally, adding four up-spins (bosons) at p_1 , p_4 , p_7 , and p_{10} leads to a Fock state consistent with a quantum drum with five plaquettes connected by vertices (Fig. 4, left panel, group labelled by ④). To illustrate possibility (ii), we can add four up-spins (bosons) at p_1 , p_3 , p_7 and p_{11} (Fig. 4, left panel) which leads to a Fock state consistent with a single-plaquette quantum drum containing sites p_6 , p_7 and p_8 while the other up-spins (bosons) become inert. To illustrate possibility (iii), we can add a single up-spin (boson) at p_5 (Fig. 4, left panel) to generate a Fock state that has only inert up-spins (bosons).

This recursive procedure can be carried forth for the bigger quantum drums to produce more complicated quantum drums. An example is shown in panel marked as B (Fig. 4, right panel) where three up-spins (bosons), indicated by filled black dots, are placed on the boundary of the shielding region of a quantum drum, previously produced by adding two up-spins (bosons) at the boundary of the shielding region of the elementary single-plaquette drum, which leads to a bigger quantum drum with ten elementary plaquettes that are connected by edges. In principle, this recursive procedure can be used to generate and enumerate all possible quantum drums until a given stage of the recursion starting from the most elementary one-plaquette drum, but we leave this for a possible future investigation.

2.1.4 Wires, junctions of wires, other quasi-1D and 2D drums

As is already evident from the examples that we have constructed so far, quantum drums come in several shapes and sizes, from being composed of a single elementary plaquette (Fig. 1) to a finite number of plaquettes (Fig. 1, Fig. 2, Fig. 4). One can even construct quantum drums with an arbitrarily large number of plaquettes in the thermodynamic limit. These varieties of drums can be quasi-1D or 2D in nature. We dub the *simplest* quasi-1D drum as a wire. A wire is composed of N_p plaquettes that share vertices along a single diagonal and resemble straight wires (see Fig. 4, left panel for three such drums with $N_p = 1, 2, 3$). Such a wire can be constructed with any $N_p \geq 1$ that leads to a quasi-1D structure for $N_p \gg 1$. Interestingly, one can create other quantum drums that resemble different kinds of junctions of such wires. Examples of such quantum drums are shown in Fig. 5. In the top panel, the quantum drums marked by A and B can be viewed as two different junctions of two wires, while in the bottom panel, the quantum drum marked by C (D) can be viewed as a junction of three (four) quantum wires. Wires can be used to build still more intricate quasi-1D as well as 2D drums (see Sec. 3.2 for details). The fragment sizes for large quasi-1D (2D) drums scale as $\alpha^l \times \alpha^l$ ($\beta^{l^2} \times \beta^{l^2}$) where $\alpha > 1$ ($\beta > 1$) as $l \gg 1$ where l represents the linear dimension of the drum and α (β) depend on the nature of the quantum

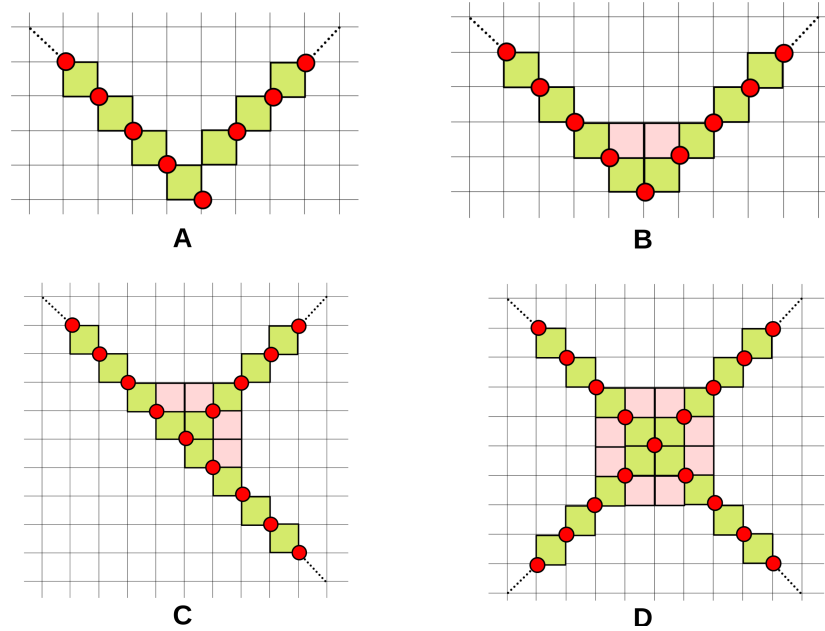


Figure 5: The quantum drums marked from A-D can be viewed as examples of different kinds of junctions of wires. A and B show examples of junctions of two wires while C (D) shows an example of a junction of three (four) wires. The green (pink) plaquettes in all the quantum drums follow the same convention as used in Fig. 1. The filled red dots indicate up-spins in all the panels and represent just one of the many possible Fock states of the corresponding drum.

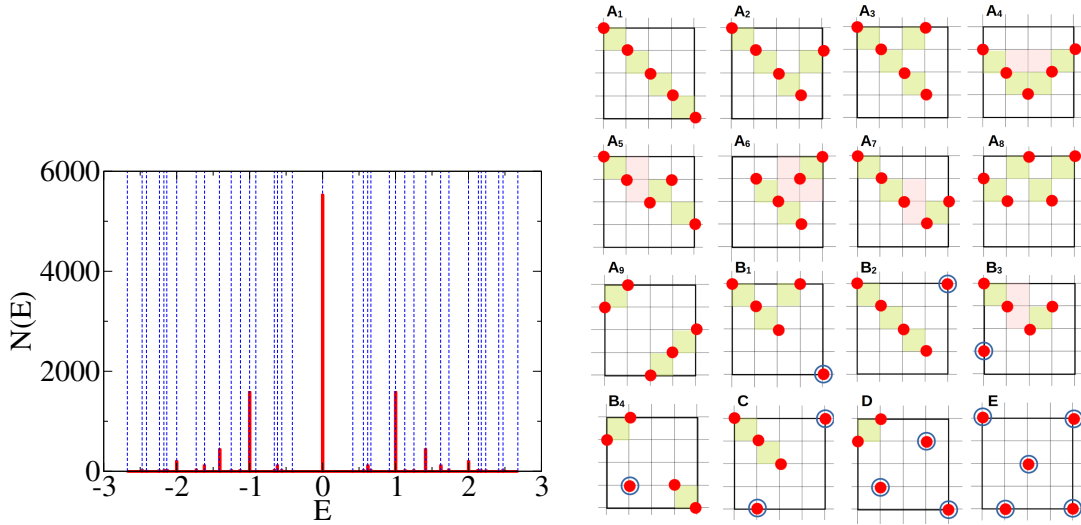


Figure 6: (Left panel) Histogram of the energy eigenvalues for a 5×5 lattice with 5 up-spins and OBC. The vertical dotted blue lines indicate the allowed eigenvalues from Eq. 8. (Right panel) The allowed quantum drums in this system where the up-spins (bosons) are indicated by filled red dots and the plaquettes that belong to quantum drums are shaded. The green (pink) plaquettes in all the quantum drums follow the same convention as used in Fig. 1. The inert up-spins (bosons) are indicated by a blue circle around the filled red dot. Each quantum drum is consistent with more than one Fock state with only one representative Fock state shown here. The different eigenstates can be viewed as modes of these quantum drums.

drum under consideration. Each such quantum drum can be viewed as an interesting example of an interacting quasi-1D/2D model with a constrained Hilbert space that also satisfies an internal subsystem symmetry of simultaneous conservation of magnetizations along each column and each row of the drum, where the columns/rows are defined with respect to the $L_x \times L_y$ lattice in which the drum is embedded, when only the sites that belong to the drum are considered.

2.2 Exact diagonalization of small lattices and deciphering spectrum using drums

The constrained nature of the Hilbert space reduces the number of allowed Fock states from 2^{L^2} to κ^{L^2} where $\kappa \approx 1.503 \dots$ is the hard square entropy constant [74] for a square lattice with $L \gg 1$. This growth of the Hilbert space dimension with L is, nonetheless, still too large to perform ED for the full spectrum for even moderately large values of L . However, analysing the numerical results for small $L \times L$ lattices is already instructive.

Let us first consider a 5×5 lattice and focus on the total magnetization sector with 5 up-spins (bosons). This gives a Hilbert space dimension of 10741 from direct enumeration taking the hard-core constraints in account. Plotting the histogram of the energy eigenvalues obtained from full ED reveals that the eigenvalues are clustered around only a few special values (up to machine precision) (Fig. 6, left panel) unlike what is expected of a generic interacting system with a similar Hilbert space dimension. Furthermore, while an explicit construction shows that there are 4559 inert Fock states that are trivially annihilated by H (Eq. 1) in this magnetization

sector, ED reveals that there are a total of 5525 zero modes (with zero eigenvalue within machine precision) implying the presence of 966 non-trivial zero modes. ED also shows the presence of 1580 eigenmodes with eigenvalue $+1$ (-1) and 196 eigenmodes with eigenvalue $+2$ (-2). Such non-zero integer eigenvalues are unexpected in generic interacting models which have highly irrational eigenvalues that cannot be expressed in any simple closed form.

These and other features of the full ED data can be completely understood in terms of quantum drums (Fig. 6, right panel). The 10741×10741 matrix for H in the computational basis gets fragmented into 4559 (1×1), 1552 (2×2), 434 (3×3), 324 (4×4), 32 (5×5), 32 (6×6), 16 (7×7) and 2 (8×8) Hilbert space fragments. The 1×1 fragments simply correspond to the inert Fock states that are annihilated by all local terms of H (Eq. 1) (and are denoted collectively by panel marked E in Fig. 6, right panel). All the other fragments can be viewed as being generated from a collection of appropriate quantum drums and any remaining inert up-spins (bosons) that are not part of any drum. Given the lattice dimensions and the number of up-spins (bosons), only certain drums are allowed with specific degeneracies set by the lattice. All 2×2 fragments are generated by a quantum drum with two up-spins (bosons) on an elementary plaquette and the rest of the 3 up-spins (bosons) being inert (these are represented collectively by panel marked D in Fig. 6, right panel). Given the lattice dimension, there are 1552 distinct ways of choosing the drum plaquette and the 3 inert up-spins (bosons) which explains the notation $D[1552]$ used in Eq 8. The 3×3 fragments are generated by 128 B3-type quantum drums and 306 C-type quantum drums, where the former drum is composed of 4 up-spins (bosons) while the latter drum is composed of 3 up-spins (bosons) while the rest of the up-spins are inert ((these two cases are represented collectively by panels marked B3 and C in Fig. 6, right panel). It is useful to stress here that while the B3-type and C-type drums are evidently different from each other, they have identical spectra (Eq. 8). The 4×4 fragments are generated by 8 A5-type, 16 A6-type, 8 A7-type, 96 B1-type and 196 B4-type quantum drums. While A5, A6, and A7-type drums contain 5 up-spins (bosons), B1 and B4-type drums contain 4 up-spins (bosons) (these are represented collectively by panels marked A5, A6, A7, B1, and B4 in Fig. 6, right panel). A5, A7 and B1-type quantum drums have identical spectra even though these three types of drums are distinct from each other. The 5×5 fragments are generated by 12 A8-type and 20 B2-type quantum drums (these are represented collectively by panels marked A8 and B2 in Fig. 6, right panel). The 6×6 fragments are generated by 16 A3-type, 12 A4-type and 4 A9-type quantum drums (these are represented collectively by panels marked A3, A4, and A9 in Fig. 6, right panel). Lastly, the 7×7 (8×8) fragments are generated by 16 (2) A2 (A1)-type quantum drums (these are represented collectively by panels marked A1 and A2 in Fig. 6, right panel). The eigenspectra of all the fragments that arise from these quantum drums, barring A2-type drums, can be expressed in closed form and show a variety of eigenvalues including zero modes, non-zero integer modes and irrational modes (Eq. 8). The extra non-trivial zero modes and their degeneracies can also be understood as zero modes of quantum drums like A1, A2, A3, A4, A6, A8, B2, B3, B4 and C (Eq. 8).

$$\begin{aligned}
 A1[2] &\rightarrow (\pm\sqrt{4+\sqrt{10}}, \pm\sqrt{2}, \pm\sqrt{4-\sqrt{10}}, 0, 0) \\
 A2[16] &\rightarrow (\pm 2.47367\dots, \pm 1.25235\dots, \pm 0.559107\dots, 0) \\
 A3[16] &\rightarrow (\pm\sqrt{3+\sqrt{3}}, \pm\sqrt{3-\sqrt{3}}, 0, 0) \\
 A4[12] &\rightarrow (\pm\sqrt{5}, \pm 1, 0, 0) \\
 A5[8], A7[8], B1[96] &\rightarrow \left(\pm\frac{1}{2}(1 \pm \sqrt{5})\right) \\
 A6[16] &\rightarrow (\pm\sqrt{3}, 0, 0) \\
 A8[12] &\rightarrow (\pm\sqrt{3}, \pm 1, 0) \\
 A9[4] &\rightarrow (\pm(1 \pm \sqrt{2}), \pm 1) \\
 B2[20] &\rightarrow \left(\pm\sqrt{\frac{1}{2}(5 \pm \sqrt{17})}, 0\right) \\
 B3[128], C[306] &\rightarrow (\pm\sqrt{2}, 0) \\
 B4[196] &\rightarrow (\pm 2, 0, 0) \\
 D[1552] &\rightarrow \pm 1, \quad E[4559] \rightarrow 0
 \end{aligned} \tag{8}$$

The degeneracies associated with the different quantum drums indicated inside [] for each case in Eq. 8 arise from the number of distinct ways in which such drums can be placed on the 5×5 lattice with OBC. For example, A1 has a degeneracy of two because there are two diagonals along which such a drum may be placed. Similarly, A2 has a degeneracy of sixteen since there are sixteen distinct ways to place a ‘‘L’’ composed of four connected plaquettes on this lattice. The other degeneracies given in Eq. 8 can be computed similarly.

2.3 Eigenstates with integer energies from packing of one-plaquette drums

Eigenstates composed of only elementary one-plaquette quantum drums and inert spins already generate non-trivial zero modes and non-zero integer eigenvalues. These can be viewed as the 2D generalization of bubble eigenstates discussed in a 1D model of Hilbert space fragmentation [64]. Hilbert space fragments with n_0 such independent one-plaquette drums have a dimensionality of 2^{n_0} since each such elementary quantum drum is consistent with two configurations on the plaquette. An extensive number of such elementary quantum drums are needed to form finite energy-density eigenstates of H with a macroscopic number of up-spins (bosons) (Fig. 7). The closest packing of these elementary quantum drums such that the boundaries of their shielding regions do not overlap is shown in Fig. 7 which yields the maximum possible value of $n_0 = L^2/9$ for a $L \times L$ square lattice when $L \gg 1$ thus fixing the corresponding fragment’s dimension to be equal to

$$(2^{1/9})^{L^2} \approx (1.08006\dots)^{L^2}. \tag{9}$$

The corresponding matrix can be immediately diagonalized by noting that the form of H projected to any $n_0 \neq 0$ fragment produced solely by elementary one-plaquette quantum drums equals

$$H_{\text{eff}} = \sum_{i=1}^{n_0} \tau_i^x \tag{10}$$

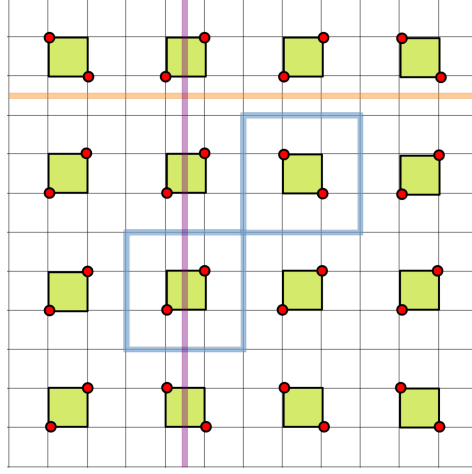


Figure 7: Close packing of elementary one-plaquette quantum drums shown, where the drum plaquettes are shaded, alongwith the boundaries of the shielding regions for two such drums (shown as thick blue lines). An initial Fock state which is consistent with this arrangement of quantum drums and where up-spins (bosons) are indicated by filled red dots is also shown.

where i denotes the center of an elementary drum plaquette, and τ_i^x locally flips an arrangement of $(+1, -1, +1, -1)$ to $(-1, +1, -1, +1)$ and vice-versa on that drum in the computational basis. This “non-interacting” H_{eff} only leads to integer eigenvalues for any n_0 . If n ($n_0 - n$) of the elementary quantum drums are associated with an eigenvalue $\tau_i^x = +1(-1)$, the resulting eigenstate has energy $E = 2n - n_0$. Clearly, there are $\binom{n_0}{n}$ distinct eigenstates that have the same energy $E = 2n - n_0$. Assuming that both $n_0, n \gg 1$, the degeneracy $\Omega(n)$ of such eigenstates is bounded below by

$$\Omega(n) > 2^{n_0} \sqrt{\frac{2}{\pi n_0}} \exp\left(2n_0 \left(x - \frac{1}{2}\right)^2\right) \quad (11)$$

where $n_0 = L^2/9$ for the largest such fragment (Fig. 7) and $x = n/n_0$. This bound immediately shows that the number of such integer eigenstates is exponentially large in the system size for integer energies that range from $E = 0$ to $|E| \sim O(L)$ (while the maximum value of the integer energy $|E| = L^2/9$ when $L \gg 1$ for a $L \times L$ square lattice with OBC). These high-energy eigenstates satisfy a strictly area law scaling of entanglement entropy with the entanglement entropy of an arbitrary bipartition, $S_{\text{bp}} = bL$, where b can range from 0 to $\ln(2)/3$ (examples of two such bipartition cuts which give the extreme values of b are shown as thick lines in Fig. 7), depending on the nature of the bipartition.

Any Fock state consistent with n_0 independent one-plaquette drums (e.g., one such Fock state is shown in Fig. 7 where the red filled dots represent up-spins (bosons)) shows persistent oscillations with a time-period $T = \pi$ under unitary evolution under H for a class of local operators. This can be directly related to the non-interacting nature of H_{eff} in Eq. 10 which leads to the following emergent dynamical symmetry [75]:

$$\left[P_{\text{eff}} H P_{\text{eff}}, \frac{\tau_i^y + i\tau_i^z}{2} \right] = \omega \left(\frac{\tau_i^y + i\tau_i^z}{2} \right) \quad (12)$$

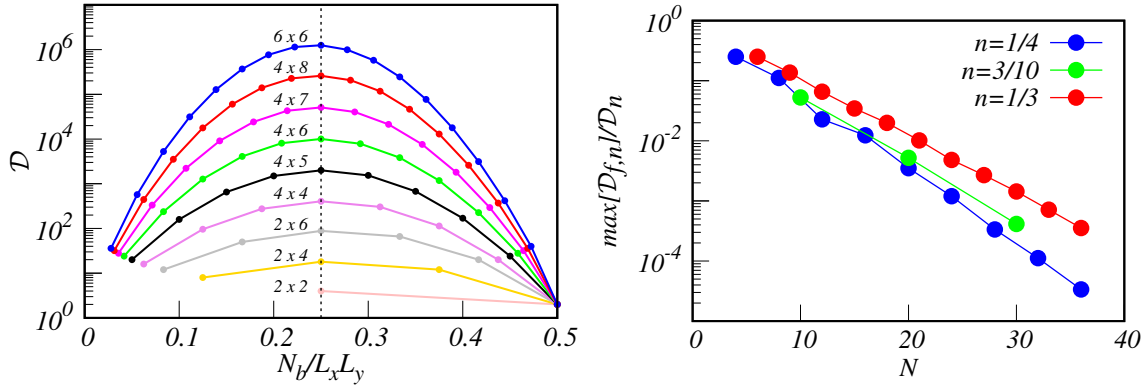


Figure 8: (Left panel) The total Hilbert space dimension \mathcal{D} as a function of the number of up-spins, N_b , for rectangular lattices $L_x \times L_y$ of various dimensions. The thin dotted vertical line is at $n = N_b/(L_x L_y) = 1/4$. (Right panel) The behavior of the ratio of the dimension of the largest Hilbert space fragment and the total Hilbert space dimension for the magnetization sector for densities $n = 1/4$ (blue), $n = 3/10$ (green) and $n = 1/3$ (red) shown for rectangular lattices with dimension $L_x \times L_y$ and OBC as a function of the system size $N = L_x L_y$.

where P_{eff} is a projection operator to the Fock space with n_0 one-plaquette drums and $\omega = 2$ given the form of H_{eff} in Eq. 10. Thus, for any such initial Fock state, any local operator with a finite overlap with any of the $\left(\frac{\tau_i^y + i\tau_i^z}{2}\right)$ operators will show persistent oscillations with a time period $T = 2\pi/\omega = \pi$.

3 Strong Hilbert space fragmentation

In this section, we show strong Hilbert space fragmentation for this kinematically constrained 2D model (Eq. 2) defined on a $L_x \times L_y$ rectangular lattice with OBC as $L_x, L_y \gg 1$. We first discuss numerical evidence from ED in Sec. 3.1. In Sec. 3.2, we introduce a decomposition of quantum drums in terms of parallel wires which reveals how to construct quantum drums with the largest fragment dimension, given a fixed number of up-spins (bosons). The construction of some 2D quantum drums with large fragment dimensions and the lack of thermalization for typical initial product states with an extensive number of up-spins (bosons) will be discussed in Sec. 3.3.

3.1 Numerical evidence from exact diagonalization

One procedure to distinguish between weak and strong fragmentation [50,51] involves monitoring the ratio of the largest Hilbert space fragment (denoted by $\max[\mathcal{D}_{f,n}]$) to the total Hilbert space dimension (denoted by \mathcal{D}_n) in a sector with a *fixed* density (denoted by n) of up-spins (bosons) for different system sizes. We stress here that only the global symmetry of total magnetization conservation and its associated density is relevant for this analysis since internal symmetries like reflections etc can always be removed by adding suitable diagonal terms to H in the computational basis that do not connect the different Hilbert space fragments. If the ratio $\max[\mathcal{D}_{f,n}]/\mathcal{D}_n$ behaves

as $\exp(-\gamma N)$ with $\gamma > 0$ as the number of sites in the system, N , diverges, it implies strong fragmentation; in contrast, if it approaches 1 as $N \gg 1$, it implies weak fragmentation.

Using exact enumeration techniques, we calculate the Hilbert space dimension, \mathcal{D} , for a fixed number of up-spins (bosons), N_b , for a variety of rectangular lattices of dimension $L_x \times L_y$ with OBC (see Fig. 8, left panel) which shows that \mathcal{D} is maximized when $n = N_b/(L_x L_y) = 1/4$. We then focus on this particular density of up-spins (bosons) $n = 1/4$ as well as two other densities $n = 3/10$ and $n = 1/3$ to show the scaling of $\max[\mathcal{D}_{f,n}]/\mathcal{D}_n$ for fixed n as a function of $N = L_x L_y$ in Fig. 8, right panel using data from exact enumeration. The data for these limited system sizes already clearly indicate that $\max[\mathcal{D}_{f,n}]/\mathcal{D}_n \sim \exp(-\gamma N)$ with γ depending on the density of up-spins (bosons), n , and thus points towards strong Hilbert space fragmentation in this 2D model.

3.2 Wire decomposition of quantum drums

As already introduced earlier, wires represent the basic quantum drums that can be generated for any given number of plaquettes, N_p , by arranging the plaquettes in a vertex-sharing pattern along any one of the two diagonal directions of the parent $L_x \times L_y$ lattice. A *reference Fock state* of the wire can be taken to be all the $N_p + 1$ up-spins (bosons) to be arranged along the length of the drum. The shielding region around a wire consists of all plaquettes that share either an edge or a vertex with any of the N_p plaquettes that belong to the drum. As we will show here, a reference Fock state for more complicated drums can be constructed from two or more parallel wires with differing lengths in general. Each of these wires can be initialized in its reference state where the wires are placed close enough such that they cannot fluctuate independently. This, in turn, indicates that the boundaries of their shielding regions cross. We refer the reader to Sec. 4.2 (Sec. 5) where the spectrum for wires with small (large) N_p shall be discussed. For now, it is sufficient to note that the number of Fock states generated by a wire with N_p plaquettes equals F_{N_p+2} (a Fibonacci number) where $F_0 = 0$, $F_1 = 1$, and $F_n = F_{n-1} + F_{n-2}$ for $n > 1$ (see Sec. 5.2 for the derivation).

In this section, we will show that

1. Drums composed of only vertex-sharing plaquettes can be generated by parallel wires that can all fluctuate *simultaneously* being at a distance of $2\sqrt{2}$ in lattice units from each other. All the Fock states of such drums can be generated from the fluctuations of these parallel wires and possibly, other sets of parallel wires in the same direction or perpendicular to the direction of the original set of wires.
2. Drums composed of only edge-sharing plaquettes can be generated by parallel wires that *cannot* fluctuate simultaneously being at a distance of $(3/2)\sqrt{2}$ in lattice units from each other, but only do so if alternate wires are kept in their reference states. The Fock states of such drums can be generated from the fluctuations of the alternate parallel wires and possibly, other sets of alternate parallel wires in the same direction or perpendicular to the original set of wires. However, not all simultaneous fluctuations of such consecutive wires are disallowed and these can be represented as *additional* excitations of elementary plaquettes that are separated by 3 lattice units along x or y such that these plaquettes can fluctuate *simultaneously*.
3. Drums with both edge-sharing as well as vertex-sharing plaquettes can be built from parallel wires such that while all the wires cannot fluctuate simultaneously, some consecutive wires can do so if the other wires are kept in their reference state.

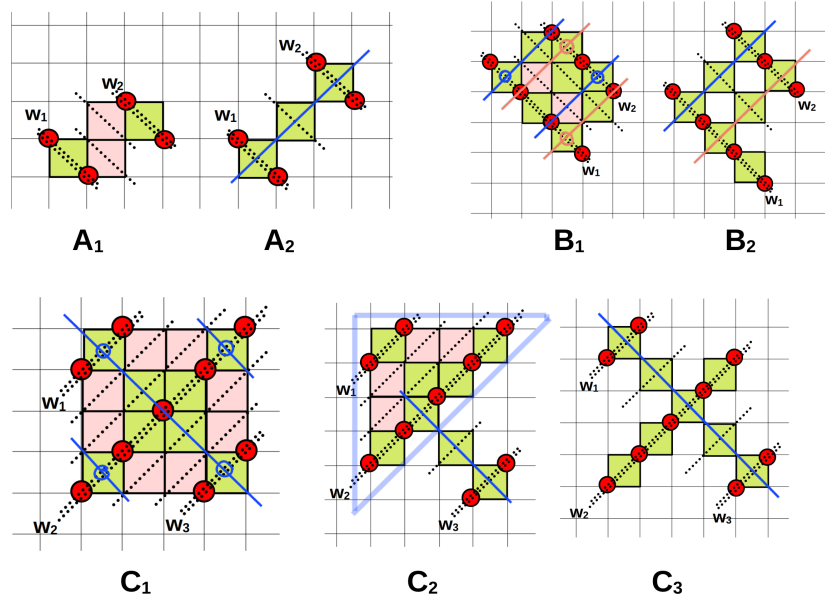


Figure 9: Examples of wire decomposition of quantum drums shown here. The drums labeled A_1 and A_2 can be constructed from two parallel wires both with $N_p = 1$, the drums labeled B_1 and B_2 can be constructed from two parallel wires with $N_p = 3$ and $N_p = 2$ while the drums labeled C_1 , C_2 , and C_3 can be constructed from three parallel wires, where two of them have $N_p = 1$ and one has $N_p = 4$. The wires in all the panels are indicated by double dashed lines and also labeled by w_1 , w_2 , w_3 . The red filled dots in all panels represent up-spins (bosons). The perpendicular wires that can be generated from the Fock state shown for each drum are indicated by bold lines in blue and orange. Additionally, the plaquettes marked by open blue (orange) circles at their centers in B_1 and C_1 represent the locations of one-plaquette excitations that generate additional Fock states that cannot be represented by excitations of alternate parallel wires in these two cases. In the drum C_2 , a smaller drum made of 10 edge-sharing plaquettes (indicated by thick blue region enclosing it) fluctuates simultaneously, with the wire w_3 . The green (pink) plaquettes in the drums shown in all panels follow the same convention as used in Fig. 1.

We start with the simplest case of two $N_p = 1$ wires in their reference state that are placed parallel to each other. If such wires fluctuated independently, then the two independent quantum drums would have produced a total of $F_3 \times F_3 = 4$ Fock states. There are two distinct ways of placing these wires with respect to each other such that they do not fluctuate independently and no inert up-spins (bosons) are created. These are shown as the quantum drums marked by A_1 and A_2 in Fig. 9. While the drum A_1 generates a Hilbert space fragment with 3 Fock states, which is less than the fragment size from two independently fluctuating $N_p = 1$ wires, the drum A_2 generates one with 5 Fock states, which is more than the fragment size from two independently fluctuating $N_p = 1$ wires. In the drum indicated by A_1 (Fig. 9), the wire w_1 (w_2) (indicated by double dotted lines in Fig. 9) can fluctuate to generate both its Fock states only if w_2 (w_1) is held fixed in its reference state. Thus, the two wires w_1 and w_2 *cannot* fluctuate simultaneously in A_1 and produce $2F_3 - 1 = 3$ states. On the other hand, in the drum A_2 (Fig. 9), both the wires w_1 and w_2 (indicated by double dotted lines in Fig. 9) *can* fluctuate simultaneously without producing a Fock state that violates the hard-core constraints. Additionally, performing a ring-exchange from the reference state on both the plaquettes that represent w_1 and w_2 generates the reference state for another wire with $N_p = 3$ that is *perpendicular* to w_1 and w_2 (shown as a blue line in the drum marked A_2 in Fig. 9). The Fock state obtained from a ring-exchange on the middle plaquette from the reference state of this $N_p = 3$ wire cannot be represented by combining any of the Fock states generated from the w_1 and w_2 wires and accounts for the total $F_3^2 + 1 = 5$ Fock states for the drum A_2 . In the case of A_1 [A_2], the minimum distance between the parallel wires w_1 and w_2 equals $(3/2)\sqrt{2}$ [$2\sqrt{2}$] in lattice units (Fig. 9).

The drums labeled B_1 and B_2 in Fig. 9 represent more complicated cases that arise when two parallel wires in their reference states, one with $N_p = 3$ and another with $N_p = 2$, are brought close to each other such that the minimum distance between the wires equal $(3/2)\sqrt{2}$ and $2\sqrt{2}$ respectively. If these two wires fluctuated independently, these would have generated $F_5 \times F_4 = 15$ Fock states. However, the drum B_1 generates a fragment with 11 Fock states while the drum B_2 generates a fragment with 18 Fock states. In the drum B_1 (Fig. 9), the wire w_1 (w_2), shown by double dotted lines in Fig. 9, can fluctuate to generate all its Fock states only if the other wire w_2 (w_1) is held fixed in its reference state. Such wire fluctuations lead to $F_5 + F_4 - 1 = 7$ states. Two cases where fluctuations of a perpendicular wire (indicated by the top blue line and the bottom orange line respectively in the drum marked B_1 in Fig. 9) when the other wire parallel to it at a distance $(3/2)\sqrt{2}$ (indicated by the bottom blue line and the top orange line respectively in Fig. 9) is kept fixed in its reference states generates an additional 2 Fock states. The remaining 2 Fock states in the fragment are generated by two separate cases of ring-exchanges on two plaquettes together [indicated by the plaquettes with an open circle of the same color (blue and orange) at their centers] that are separated by 3 lattice units along x/y as shown in Fig. 9 (panel marked B_1). On the other hand, in the drum B_2 (Fig. 9), both the wires w_1 and w_2 (indicated by double dotted lines in Fig. 9) can fluctuate simultaneously to generate all their Fock states without violating the hard-core constraints. Fluctuations of w_1 and w_2 in the drum B_2 cannot, however, generate any Fock state with two up-spins (bosons) along the diagonal parallel to w_1 , w_2 on any of the two plaquettes that are not part of w_1 and w_2 . The extra $18 - F_5 \times F_4 = 3$ Fock states are generated from ring-exchange moves in any one of these two plaquettes starting with Fock states obtained from the fluctuations of w_1 and w_2 that can be represented as the reference state of a $N_p = 3$ wire perpendicular to both w_1 and w_2 and containing one of these two plaquettes (shown by a blue and an orange line perpendicular to w_1 , w_2 in Fig. 9).

Finally, we consider a case where three parallel wires in their reference states, w_1 with $N_p = 1$,

w_2 with $N_p = 4$, and w_3 with $N_p = 1$, are brought close to each other to generate three different drums labeled C_1 , C_2 , and C_3 in Fig. 9. While independent fluctuations of these three wires generate $F_3 \times F_6 \times F_3 = 32$ Fock states, the fragment generated by the drum C_1 contains 24 Fock states, by the drum C_2 contains 28 Fock states, and by the drum C_3 contains 42 Fock states, respectively. In the drum C_1 (Fig. 9), the wire w_1 (w_3) can only access all its Fock states if w_2 is held fixed in its reference state (with these wires indicated by double dotted lines in the drum C_1 in Fig. 9). Similarly, the wire w_2 can only access all its Fock states if both w_1 and w_3 are fixed to their reference states in C_1 . This generates a total $F_3^2 + F_6 - 1 = 11$ Fock states. An additional 5 Fock states of drum C_1 are generated by similar wire fluctuations of parallel wires separated by $(3/2)\sqrt{2}$ but perpendicular to w_1, w_2, w_3 (indicated by blue lines in drum C_1 in Fig. 9). Finally, the remaining 8 Fock states in C_1 are generated by simultaneous ring-exchanges on two/three of the four corner plaquettes (marked by blue circles at the centres of the corresponding plaquettes in C_3 in Fig. 9) that are separated from each other/from a corner plaquette by 3 lattice units in the x/y direction. On the other hand, in the drum C_3 (Fig. 9), all the wires, w_1, w_2 and w_3 (indicated by double dotted lines in Fig. 9), can fluctuate simultaneously without violating the hard-core constraints. Furthermore, fluctuations in w_1, w_2 and w_3 generates a new open channel of fluctuations in the form of a wire with $N_p = 5$ plaquettes in the direction perpendicular to these wires (indicated by a blue line in C_3 in Fig. 9) which generates an additional 10 Fock states besides the $F_3 \times F_6 \times F_3 = 32$ Fock states generated from w_1, w_2, w_3 . The drum marked as C_2 in Fig. 9 represents an interesting intermediate case between C_1 and C_3 where the parallel wires w_1 and w_2 (w_2 and w_3) are at a distance $(3/2)\sqrt{2}$ ($2\sqrt{2}$) from each other. The smaller drum containing wires w_1, w_2 and composed of 10 edge-sharing plaquettes (marked by the blue region in the drum C_2 in Fig. 9) can fluctuate simultaneously with the wire w_3 . This leads to a total of $13 \times 2 = 26$ Fock states (see Fig. 16 for the 13 Fock states of the smaller drum made by the wires w_1 and w_2). The additional states are generated from an extra open channel for fluctuations along a $N_p = 3$ wire perpendicular to w_1, w_2, w_3 containing the w_3 plaquette as its right-most plaquette as indicated by the blue line perpendicular to w_1, w_2, w_3 in the drum C_2 in Fig. 9. This results in 2 Fock states where a ring-move is performed on the reference state of this $N_p = 3$ wire using the plaquette excluded from both the smaller drum composed of 10 edge-sharing plaquettes and w_3 .

These examples demonstrate the general principle that given n parallel wires, with unequal lengths in general, it is optimal to place the wires such that all the parallel wires can fluctuate simultaneously and that these fluctuations additionally generate the maximum number of longest-possible wires perpendicular to the original wires as extra open channels of fluctuations to maximize the fragment size generated by the resulting drum. Both these conditions are satisfied by appropriate drums composed of only vertex-sharing plaquettes as shown in Fig. 9 (panels marked A_2, B_2 and C_3).

The fact that drums with only vertex-sharing plaquettes are generated when the parallel wires can simultaneously fluctuate can be most clearly seen by using the overlap of the shielding regions of different parallel wires (see Fig. 10) to construct the drums shown in Fig. 9. For the drums A_1, A_2, B_1, B_2 and C_3 , it is sufficient to consider the overlap of the shielding regions of the parallel wires shown in Fig. 9 as can be seen from Fig. 10, where the overlapping plaquettes of the shielding regions have been denoted by “o” in all panels of Fig. 10. The drums C_1 and C_2 present more interesting cases where this construction only identifies a subset of plaquettes that belong to the corresponding drum (Fig. 10). However, starting from the reference state of the original parallel wires, it is easy to perform ring-exchange moves on a subset of the plaquettes that belong to these wires to create a Fock state that can be viewed as parallel wires in their reference state, but in the perpendicular direction to the original wires (Fig. 10). The overlap of the shielding regions of

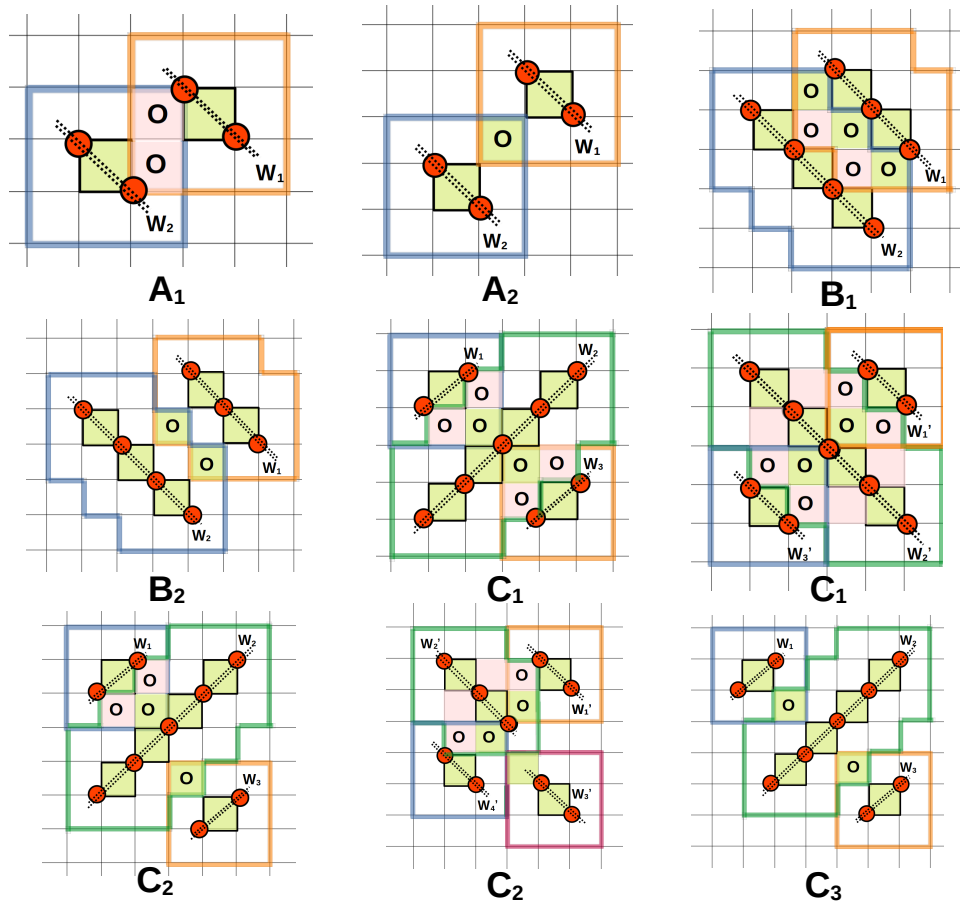


Figure 10: The drums A_1 to C_3 shown in Fig. 9 can be constructed using the overlap of the shielding regions of parallel wires as shown. The wires are indicated by double dashed lines in each panel. The red filled dots in all panels represent up-spins (bosons). The boundaries of the shielding region of each wire is shown using thick lines of different colors and the plaquettes formed by the overlap of the shielding regions are indicated by “o”. The green (pink) plaquettes in the drums shown in all panels follow the same convention as used in Fig. 1.

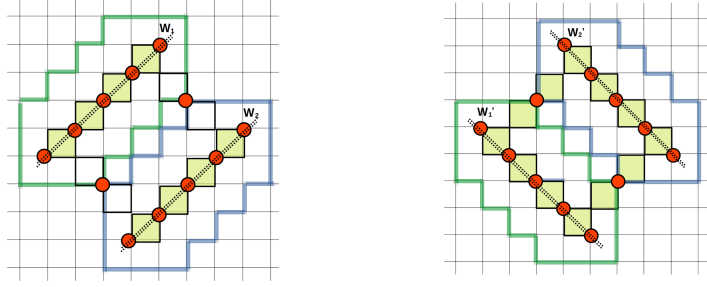


Figure 11: Two parallel wires w_1 and w_2 (see left panel) and two other parallel wires w'_1 and w'_2 (see right panel) indicated by double dotted lines, both in their reference state and both with $N_p = 4$, separated by a distance of $3\sqrt{2}$ in lattice units. The wires w_1, w_2 are perpendicular to the wires w'_1, w'_2 . In both panels, two up-spins (bosons) are located on two common sites between the boundaries of the shielding regions, shown using thick lines, of the wires. The red filled circles in both panels indicate up-spins. The green plaquettes in the drums shown in both panels follow the same convention as used in Fig. 1, with the right panel showing all the plaquettes that belong to this drum.

these new wires gives the remaining plaquettes that are part of the quantum drum for both C_1 and C_2 (Fig. 10). Given that all the parallel wires can fluctuate simultaneously but not independently, the overlap of the shielding regions only generate vertex-sharing plaquettes with the parallel wires being separated by a distance of $2\sqrt{2}$ in terms of lattice units. Finally, stacking two parallel wires even closer such that these are at a distance of $\sqrt{2}$ in terms of lattice units freezes both the wires in their reference states. Hence, the last category of wire arrangements, where any two parallel wires are only separated by $\sqrt{2}$, are not relevant for constructing quantum drums.

For completeness, we note that if two parallel wires are separated by a distance of $3\sqrt{2}$, but no more, these wires can still be coupled to each other to make a larger drum by placing up-spins (bosons) in a subset of the common sites between the boundaries of the shielding regions of both the wires. An example of this is illustrated in Fig. 11 where two parallel wires w_1 and w_2 , both with $N_p = 4$ and in their reference state, are placed at a distance of $3\sqrt{2}$ from each other (Fig. 11, left panel). Two up-spins (bosons) are placed on two of the common sites of the boundaries of the shielding regions of both the wires (the boundaries of the shielding regions are shown using thick green (blue) lines for w_1 (w_2) in Fig. 11, left panel). The wires w_1 and w_2 can fluctuate simultaneously to generate all their Fock states in spite of the up-spins (bosons) on the boundaries of the shielding regions. Performing appropriate ring-exchanges on this reference state (Fig. 11, left panel), it is easy to get a Fock state that can be viewed as two parallel wires, w'_1 and w'_2 , that are both perpendicular to w_1, w_2 and again separated by $3\sqrt{2}$ with two up-spins (bosons) on two of the common sites shared by the boundaries of the shielding regions of w'_1 and w'_2 . This shows that four other plaquettes (apart from the ones shaded in Fig. 11, left panel) are part of the bigger drum and that all the Fock states can be generated from simultaneous fluctuations of either w_1, w_2 or w'_1, w'_2 , again generating a quantum drum with only vertex-sharing plaquettes.

3.3 Absence of thermalization from typical product states

We now consider the fate of typical unentangled product states in the computational basis for a large system, say a $L \times L$ lattice with OBC where $L \gg 1$. Since H (Eq. 1) is purely off-diagonal

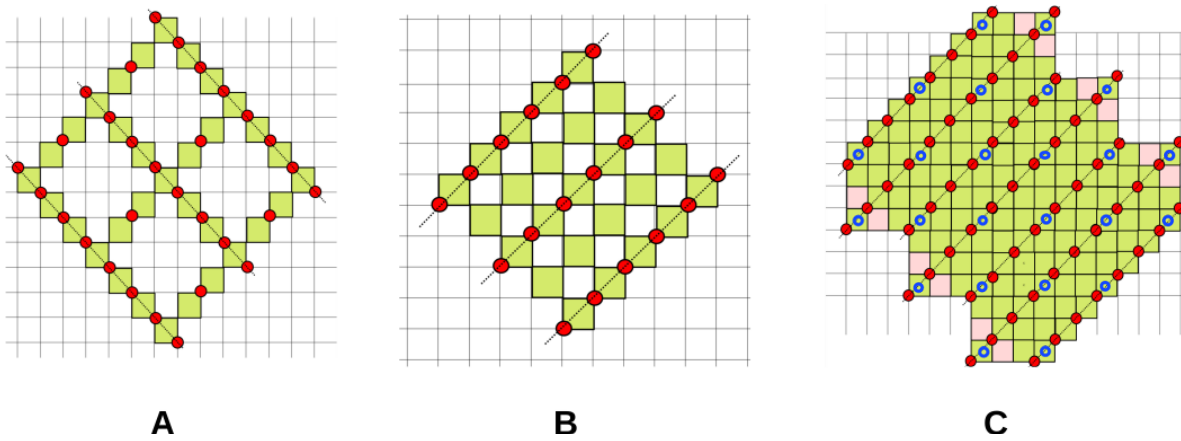


Figure 12: Three examples of 2D drums shown here. The green (pink) plaquettes in all the quantum drums follow the same convention as used in Fig. 1. The filled red dots indicate up-spins in all the panels and represent just one of the many possible Fock states of the corresponding drum. The wire decomposition of each drum is indicated by thin dotted lines in each of the three panels. Panels A and B are composed of parallel wires that can fluctuate simultaneously and hence contain only vertex-sharing plaquettes. The checkerboard drum in panel B represents the maximum packing of such wires that gives the density of up-spins (bosons) to be $1/4$. The close packed drum in panel C represents the maximum packing of wires such that none of them are inert that gives the density of up-spins (bosons) to be $1/3$. The plaquettes where ring-exchanges can be simultaneously carried out are indicated by open blue circles at their centres in panel C.

in the computational basis, all such product states have an average energy of $\langle E \rangle = 0$. Given the E to $-E$ symmetry of the many-body spectrum, ETH will imply that such a product state with a macroscopic number of up-spins (bosons) should thermalize to the infinite temperature ensemble (ITE) with the density of up-spins (bosons) fixed by the initial condition as far as local operators are concerned.

Given a product state with an extensive number of up-spins (bosons), it can be categorized in one of the following five classes:

1. The initial state is an inert Fock state which forms a 1×1 fragment on its own.
2. The initial state is consistent with a finite number of finite-sized drums, i.e., drums composed of a finite number of plaquettes, when $L \gg 1$.
3. The initial state is consistent with an extensive number of finite-sized drums when $L \gg 1$.
4. The initial state is consistent with the presence of one or more quasi-1D drums with a typical linear dimension of $O(L)$ as $L \gg 1$.
5. The initial state is consistent with the presence of one or more 2D drums with a typical linear dimension of $O(L)$ as $L \gg 1$.

Initial states in class 1 do not thermalize since all spins are inert. In class 2, an extensive number of sites do not belong to any drum and the corresponding spins are, therefore, inert and retain memory of their initial condition. Initial states in class 3 again contain an extensive number of inert down-spins when all the boundary sites of the shielding regions of the drums are considered together.

For initial states in class 4, one simply needs to consider local operators that have support from sites on opposite sides of a quasi-1D drum of linear dimension $O(L)$. Such local operators evade thermalization since all the sites that compose such a local operator cannot be part of the same quantum drum and are, therefore, dynamically disconnected and retain memory of the initial state.

Initial states in class 5 are more subtle since almost all local operators contain sites in the interior of a single 2D quantum drum. We take such a 2D quantum drum to cover (almost) the entire $L \times L$ lattice without any loss of generality. Following Sec. 3.2, a reference Fock state for such a 2D drum can be composed by bringing $O(L)$ parallel wires together, typically of length $O(L)$, in their reference states such that these wires cannot fluctuate independently. Examples of some 2D drums are shown in Fig. 12 (three panels) and in Fig. 13 (right panel).

Given that the number of Fock states accessible to a single wire of length l equals F_{l+2} (Eq. 27) where F_n are the Fibonacci numbers, the fragment size scales exponentially with increasing l as φ^l for $l \gg 1$, where $\varphi = (1 + \sqrt{5})/2 \approx 1.618 \dots$ is the golden ratio. Thus, if a 2D drum can be decomposed into parallel wires that can fluctuate simultaneously, then the corresponding number of Fock states generated equals

$$\varphi^{(L_1+L_2+L_3+L_4 \dots)} \quad (13)$$

where L_1, L_2, L_3, L_4 etc denote the lengths of these wires. Since a 2D quantum drum contains an extensive number of sites, $L_1 + L_2 + L_3 + \dots = O(L^2)$, Eq. 13 already shows that the corresponding Hilbert space fragment grows exponentially with the system size. Given a fixed density of up-spins (bosons), 2D quantum drums with the largest fragment dimensions dominate statistically,

provided that the other fragments at the same density are exponentially smaller, and control the behavior of typical initial states in class 5.

We will now consider two important cases of such 2D drums. We first consider a “checkerboard” drum (see panel B in Fig. 12) which represents the closest packing of parallel wires (indicated by dotted lines in panel B of Fig. 12) in their reference state such that all the wires can fluctuate simultaneously. Comparing the representative Fock state of this drum shown in Fig. 12 (panel B) to the inert state with the maximum density of up-spins (bosons) that equals $n = 1/2$ (Fig. 13, left panel), we see that the former may be obtained from the latter by removing the up-spins (bosons) on alternate parallel wires from the inert state. This fixes the density of up-spins (bosons) to be $n = (1/2) \times (1/2) = 1/4$ for the checkerboard drum. Since this drum only has vertex-sharing plaquettes, following Sec. 3.2 all the Fock states of this drum can be generated (in fact, overcounted) by considering simultaneous fluctuations of wires along either of the diagonal directions of the square lattice with mutual separation of $2\sqrt{2}$ and also their shifted counterparts with a shift of $\sqrt{2}$ perpendicular to the direction of the wires. This immediately establishes that

$$(\varphi^{1/4})^{L^2} < \mathcal{N}_{\text{HSD,ch}} < 4(\varphi^{1/4})^{L^2} \quad (14)$$

where $\mathcal{N}_{\text{HSD,ch}}$ equals the number of Fock states for this drum when $L \gg 1$. Thus, we get that

$$\mathcal{N}_{\text{HSD,ch}} \sim (\varphi^{1/4})^{L^2} \approx (1.12784\dots)^{L^2} \quad (15)$$

for the 2D checkerboard drum that accomodates the maximum density of simultaneously fluctuating parallel wires, resulting in a density of up-spins (bosons) that we denote as $n_{\text{ch}} = 1/4$ henceforth.

As shown in Sec. 3.2, the closest distance of approach between two parallel wires in their reference state equals $(3/2)\sqrt{2}$ in lattice units such that these do not become inert. Extending this to 2D, one gets a “close packed drum” as shown in Fig. 12 (panel C) where the parallel wires are indicated by dotted lines. Unlike the checkerboard drum, this 2D drum is composed of only edge-sharing plaquettes and its interior has no unshaded plaquettes that do not belong to the drum. The density of up-spins (bosons) for this close packed drum equals $n = 1/3$ which can be seen by comparing the reference Fock state shown in panel C of Fig. 12 to the inert state with the maximum density of up-spins (bosons), $n = 1/2$, (Fig. 13, left panel). We see that the former may be obtained from the latter by deleting the up-spins (bosons) on every two parallel wires and keeping every third wire intact from the inert state in a $1 - 0 - 0$ pattern. This gives one set of simultaneously flippable wires of the close packed drum, implying that $n = (1/6 + 1/6) = 1/3$. As discussed in Sec. 3.2, all Fock states of such structures where the consecutive parallel wires are at a distance of $(3/2)\sqrt{2}$ in lattice units can be generated from two types of excitations: (a) simultaneous fluctuations of every alternate parallel wire and (b) excitations of elementary plaquettes that are separated by 3 lattice units along x or y and thus simultaneously flippable. One set of such parallel wires (indicated by parallel dotted lines) and elementary plaquettes (indicated by open blue circles in the centers of the corresponding plaquettes) are shown in Fig. 12 (panel C). The scaling of the number of Fock states associated with the wire fluctuations can be simply calculated using Eq. 13 and gives $(\varphi^{1/6})^{L^2}$. The number of states generated from the simultaneously flippable elementary plaquettes can be calculated by simply noting that the result is identical to the one discussed in Sec. 2.3 since the elementary plaquettes have the same spatial arrangement in Fig. 7 as the marked plaquettes in Fig. 12 (panel C) thus giving the number of such excitations as $(2^{1/9})^{L^2}$ (Eq. 9). Furthermore, all the Fock states can be generated (in fact, overcounted) by

considering all combinations of such parallel wires as well as their perpendicular counterparts and the simultaneously flippable elementary plaquettes and their lattice translations. This gives that

$$(\varphi^{1/6})^{L^2} < \mathcal{N}_{\text{HSD,cp}} < 4[(\varphi^{1/6})^{L^2} + (2^{1/9})^{L^2}] \quad (16)$$

where $\mathcal{N}_{\text{HSD,cp}}$ equals the fragment dimension for this drum when $L \gg 1$. Importantly, since $2^{1/9}/\varphi^{1/6} \approx 0.996819\dots$, the above equation can be simplified to give

$$\mathcal{N}_{\text{HSD,cp}} \sim (\varphi^{1/6})^{L^2} \approx (1.08351\dots)^{L^2} \quad (17)$$

for the close packed drum that accomodates the maximum density of non-inert parallel wires, resulting in a density of up-spins (bosons) that we denote as $n_{\text{cp}} = 1/3$ henceforth.

A straightforward approach to maximize the number of states produced by wire fluctuations, given a certain density of up-spins (bosons), is to use Eq. 13 and consider 2D drums where *all* the parallel wires that compose the drums can fluctuate simultaneously which automatically lead to structures made of only vertex-sharing plaquettes. Since such wires can only have a minimum separation of $2\sqrt{2}$ in lattice units, this sets an upper bound on the density of up-spins (bosons) to be $n_{\text{ch}} = 1/4$ (the density for the checkerboard drum). For initial states in class 5 where the density of up-spins (bosons), $n \in (0, 1/4]$, vertex-sharing drums dominate statistically. An example of such a 2D drum at a lower density compared to $n = 1/4$ is shown in panel A of Fig. 12. Comparing the reference Fock state shown in panel A of Fig. 12 to the inert state with the maximum density of up-spins (bosons), $n_b = 1/2$, (Fig. 13, left panel), we see that $n = (1/6) \times (1 + 1/3) = 2/9$ for this quantum drum. The parallel wires in panel A of Fig. 12 can be obtained by deleting every two wires in the inert state and keeping every third wire intact in a 1–0–0 pattern while the up-spins that do not belong to any wire in panel A of Fig. 12 can again be obtained by taking the same 1–0–0 pattern of wires and deleting every two up-spins (bosons) and keeping every third up-spin (boson) in the surviving wires. Crucially, any 2D drum composed of vertex-sharing plaquettes alone contain an extensive number of unshaded plaquettes in its interior (Fig. 12, panels A and B) that do not belong to the drum. By definition, the two-spin local correlators $\langle (\sigma_{j_x, j_y}^z + 1)(\sigma_{j_x+1, j_y+1}^z + 1) \rangle$ and $\langle (\sigma_{j_x, j_y+1}^z + 1)(\sigma_{j_x+1, j_y}^z + 1) \rangle$ stay pinned to zero for any such unshaded plaquette during the time evolution induced by H . On the other hand, these correlators should relax to non-zero positive values at late times for the plaquettes that belong to the 2D drum assuming Krylov-restricted ETH simply because two up-spins (bosons) are allowed on both diagonals of these plaquettes. However, since H is local in space and respects translational symmetry on the lattice, the ITE at any finite density of up-spins (bosons) cannot give such an effect. Hence, typical initial states in class 5 with $n \leq 1/4$ evade ETH-predicted thermalization due to the presence of such two-spin correlators. Furthermore, while the checkerboard drum (Fig. 12, panel B) does not contain any inert spin in its interior, vertex-sharing drums with a lower density of up-spins (bosons) (e.g., Fig. 12, panel A) also contain an extensive number of sites in their interior that do not belong to the drum and thus harbor inert spins.

The thermalization properties of typical initial states in class 5 where the density of up-spins (bosons), $n \in (1/4, 1/2]$, cannot be determined by just considering 2D drums composed of vertex-sharing plaquettes. We will first show that such states always contain an extensive number of inert up-spins (bosons) for $n \in (1/3, 1/2]$. As already discussed, the close packing of parallel wires such that neighboring wires can still fluctuate generates the close packed drum (Fig. 12, panel C) and a corresponding density of $n_{\text{cp}} = 1/3$. Adding an excess amount of up-spins (bosons) in the system such that $n = (1/3) + \delta$, where $\delta \in (0, 1/6)$, necessarily leads to an extensive number of inert wires

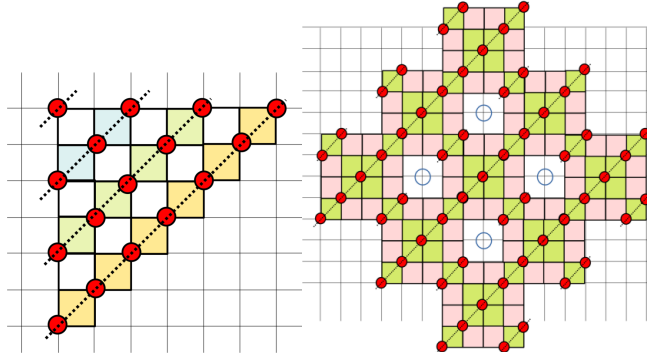


Figure 13: (Left panel) A section of the inert state with the maximum density of up-spins (bosons) equal to $1/2$ shown with the filled red dots indicating up-spins. This state can be viewed in terms of parallel wires (indicated by dotted lines and shaded plaquettes of different colors) that are placed so close that they cannot fluctuate out of their reference states. (Right panel) Example of a 2D quantum drum with a density of up-spins (bosons) between $1/4$ and $1/3$. In this particular example, the density equals $5/18$. The green (pink) plaquettes in this quantum drum follows the same convention as used in Fig. 1. The filled red dots indicate up-spins and represents just one of the many possible Fock states of the corresponding drum. The wire decomposition of the drum is indicated by thin dotted lines. The blue circles indicate inert down-spins that are not part of this quantum drum.

locked in their reference state, with the density of such wires scaling as $\delta/6$. Thus, the number of inert up-spins (bosons) in typical initial states in class 5 should scale as $\delta L^2/6$ for $n = (1/3) + \delta$ with $\delta \in (0, 1/6)$. Thus, these typical states in class 5 also evade ETH-predicted thermalization.

We now come to the case of typical initial states in class 5 where the density of up-spins (bosons) equals $n \in (1/4, 1/3)$ such that we can write $n = (1/4) + \gamma$ with $\gamma \in (0, 1/12)$. One can start with the reference state of the checkerboard drum in Fig. 12 (panel B) and insert extra parallel wires in their reference state such that the distance between parallel wires equals $\sqrt{2}$ for a linear extent of $4\gamma L$ of the system while the rest of the system still has parallel wires that can fluctuate simultaneously. However, this immediately produces $O(4\gamma L^2)$ inert up-spins (bosons) in the system and thus such initial states evade thermalization. Since the size of the spatial region that harbors wires that can simultaneously fluctuate reduces from L^2 to $(1 - 4\gamma)L^2$, the fragment size scales as $(\varphi^{\frac{1}{4}-\gamma})^{L^2}$ using Eq. 15 in this case.

There are two distinct ways of producing reference states for 2D drums with large fragment dimensions when $n \in (1/4, 1/3)$ such that an extensive number of inert up-spins (bosons) are not produced.

(i) One can have “phase-separated” drums, with the phase separation in one direction, such that different macroscopic regions are composed of close packed parallel wires in their reference state. One of these sets have parallel wires at a distance $(3/2)\sqrt{2}$ (with a local density $n = 1/3$) for a total linear extent of $(12\gamma)L$. The other regions comprise of parallel wires in their reference state at a distance $2\sqrt{2}$ (with a lower local density of $n = 1/4$) for the rest of the system to get the correct up-spin (boson) density. We refer the reader to the drum marked as C_2 in Fig. 9 for an illustration of this principle for a small drum where the parallel wires w_1 and w_2 (w_2 and w_3)

are at a distance $(3/2)\sqrt{2}$ ($2\sqrt{2}$) with respect to each other. The leading scaling for the Hilbert space size of such drums can simply be obtained by considering independent fluctuations of these “checkerboard drum” and “close packed drum” regions. Using Eq. 15 and Eq. 17, this immediately gives

$$\mathcal{N}_{\text{HSD,phase-sep}} \sim [\varphi^{1/6}]^{12\gamma L^2} [\varphi^{1/4}]^{(1-12\gamma)L^2} \sim \left(\varphi^{\frac{1}{4}-\gamma}\right)^{L^2}. \quad (18)$$

(ii) One can start with the close packed drum reference state and delete up-spins (bosons) in such a manner that another 2D drum with a lower density of up-spins (bosons) is created. We refer the reader to the 2D drum shown in the right panel of Fig. 13 where the reference Fock state of this particular drum can be produced from the reference Fock state of the close packed drum by deleting every third up-spin (boson) from alternate wires in their reference state. This gives a reduced density of up-spins (bosons) to be $(1/6)(1 + 2/3) = 5/18 \approx 0.2777\dots$ as well as an extensive density of inert down-spins from sites that are not part of the drum. However, the scaling of the fragment size for such drums is upper-bounded by $\left(\varphi^{\frac{1}{6}}\right)^{L^2}$.

Thus, the “phase-separated” drums in (i) dominate statistically for $n \in (1/4, 1/3)$ and typical initial states in class 5, that do not contain an extensive number of inert spins, nonetheless contain $O((1-12\gamma)L^2)$ unshaded plaquettes in the interior of such phase-separated drums where two-spin local correlators $\langle(\sigma_{j_x, j_y}^z + 1)(\sigma_{j_x+1, j_y+1}^z + 1)\rangle$ and $\langle(\sigma_{j_x, j_y+1}^z + 1)(\sigma_{j_x+1, j_y}^z + 1)\rangle$ stay pinned to zero for any such plaquette, thus evading ETH-predicted thermalization. This completes our analysis for the lack of ETH-predicted thermalization in typical initial states in class 5 for all $n \neq 1/3$ by considering 2D quantum drums that are statistically dominant from the wire construction. We see that such initial states have either an extensive number of inert spins or an extensive number of two-spin next-nearest neighbor correlators that are pinned to zero or both.

The case of the close packed drum with density of up-spins (bosons) $n = 1/3$ with a Hilbert space fragment whose dimension scales as $\left(\varphi^{\frac{1}{6}}\right)^{L^2}$ seems more subtle since it contains neither inert spins nor unshaded plaquettes in its bulk. In fact, initial states that arise from a wire pattern composed of $(2/3)L^2$ of the system in a checkerboard drum pattern, with a local density $n = 1/4$, and the rest of the system being fully inert with a local $n = 1/2$ also yields the same leading scaling of its fragment size as $\left(\varphi^{\frac{1}{6}}\right)^{L^2}$. We leave the issue of thermalization, or lack of it, or of an even more exotic feature like a behavior intermediate to both weak and strong Hilbert space fragmentation for the particular density of up-spins (bosons), $n = 1/3$, as an interesting open problem. For completeness, we note that ED results on small systems points towards a strong Hilbert space fragmentation scenario even at $n = 1/3$ (Fig. 8, right panel).

4 Analytical study of small quantum drums

In this section, we shall study the spectrum of the simplest quantum drums of the model analytically. We first discuss how the connection diagrams between different Fock states of a drum, where the connections are generated by H , can be represented by unidirectional trees in Sec. 4.1. Such tree structures turn out to be particularly useful in finding the non-zero matrix elements of H for large drums (e.g., see Sec. 5). We will subsequently study the case of a wire with N_p plaquettes for small N_p (Sec. 4.2), and then consider some other examples of small quantum drums that can be viewed as building blocks of the different kinds of wire junctions shown in Fig. 5 (Sec. 4.3).

4.1 Tree structure

It is convenient to represent the connection diagram between different Fock states in the Hilbert space of a drum as nodes of a tree with the non-zero matrix elements of H (which equals 1 due to the form of H in Eq. 1) between two such states denoted as a link between the corresponding nodes. Such a tree can be build in the forward direction with the different levels being denoted by integers starting from level-0 for the top level and being incremented by 1 for each of the levels below. The top level consists of a single node that can be represented by any “reference state”. It is optimal to choose a reference state such that the Fock state maximizes the number of flippable plaquettes for the corresponding drum, but this is not a necessary condition. A single application of H on this reference state at level-0 generates all the nodes at level-1, where the corresponding Fock states have exactly 1 flipped plaquette with respect to the reference state with the location of the flipped plaquette uniquely identifying the corresponding Fock state. Links are then formed between nodes at level-0 and level-1. Applying H on each of the level-1 nodes generates level-2 nodes where the corresponding Fock state has another flipped plaquette with respect to the level-1 state with the locations of the two flipped plaquettes characterizing the generated Fock state uniquely. The possibility that different level- i nodes may generate the same level- $(i + 1)$ node first arises at $i = 1$. New links are then drawn between the appropriate nodes at level-1 and level-2. This process is continued recursively at each subsequent level- i to go forward to level- $(i + 1)$ during which the links between appropriate level- i and level- $(i + 1)$ nodes are also generated. Carrying out this forward construction of the tree, one also encounters “dead nodes” which are Fock states at level- i from which no other Fock states with an extra flipped plaquette can be generated to go to the next level $(i + 1)$. The forward construction of the tree terminates when the last level is reached which is characterized by all its nodes being dead nodes. A plaquette, once flipped, cannot be unflipped in the tree construction which makes the construction unidirectional.

4.2 Wire

The simplest quantum drum of the Hamiltonian given by Eq. 1 constitutes a single plaquette ($N_p = 1$) with two up-spins (bosons) as shown in the left panel of Fig. 14. The Hilbert space of this drum constitutes two states; the Hamiltonian in the space of these two states, $|\psi_a\rangle \equiv |a\rangle$ for $a = 1, 2$, can be written as (Fig. 14)

$$H_{1\ell} = \tau^x, \quad H_{1\ell}|\psi_{1(2)}\rangle = |\psi_{2(1)}\rangle \quad (19)$$

where τ^x denotes Pauli matrix in the space of the states in the Hilbert space. This yields integer eigenvalues $E = \pm 1$.

The next set of quantum drums that we discuss constitutes two elementary square plaquettes ($N_p = 2$) with three up-spins (bosons) in total as shown in the central panel of Fig. 14. The Hilbert space consists of three states, $|\phi_a\rangle \equiv |a\rangle$ for $a = 1, 2, 3$, as shown in the panel. The action of the Hamiltonian is summarized by the tree given in the central panel of Fig. 14. In the space of these states, the Hamiltonian can be represented as

$$H_{2\ell} = \begin{pmatrix} 0 & 1 & 1 \\ 1 & 0 & 0 \\ 1 & 0 & 0 \end{pmatrix} \quad (20)$$

This yields eigenvalues $E = 0, \pm\sqrt{2}$. Thus these fragments leads to eigenenergies which can be represented by simple irrational numbers as well as a zero mode.

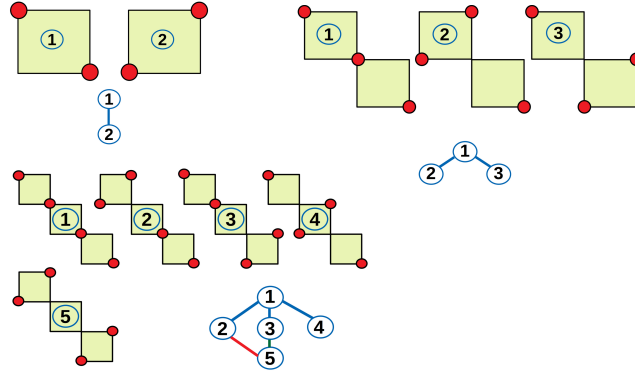


Figure 14: Left Panel:(a) Schematic representation of the basis states of the simplest fragment with $N_p = 1$ and (b) the corresponding tree between states in the Hilbert space. Center Panel: Same as the left panel but corresponding to $N_p = 2$. Right Panel: Same as the left panel but corresponding to $N_p = 3$. In all plots, the red filled dots indicates sites with up-spins (bosons). The green plaquettes in the drums follow the same convention as used in Fig. 1.

Finally, we consider a wire with $N_p = 3$ where the states have 4 up-spins (bosons). The basis states spanning the 5-dimensional Hilbert space of such a fragment is charted in the right panel of Fig. 14 and the corresponding tree is shown in the bottom panel of the figure. As can be read off from the tree, in the space of these states, the 5×5 Hamiltonian matrix can be written as

$$H_{3\ell} = \begin{pmatrix} 0 & 1 & 1 & 1 & 0 \\ 1 & 0 & 0 & 0 & 1 \\ 1 & 0 & 0 & 0 & 1 \\ 1 & 0 & 0 & 0 & 0 \\ 0 & 1 & 1 & 0 & 0 \end{pmatrix} \quad (21)$$

The corresponding eigenvalues are given by $E = 0, \pm\sqrt{5 \pm \sqrt{17}}$ leading to eigenvalues represented by non-trivial irrational numbers and a zero mode. The spectrum of these wires for larger N_p gets complicated and these shall be studied in details numerically in Sec. 5.

4.3 Junction units

In this section, we shall study small quantum drums corresponding to the simplest junction units that are building blocks of the different junctions of wires shown in Fig. 5 (A, B, C, D) and calculate their spectra analytically. Larger quantum drums that resemble a junction of two wires as shown in Fig. 5 (A) shall be studied numerically in Sec. 5.

We begin with the quantum drum corresponding to a junction of two wires as shown in Fig. 5 (A) with $N_p = 3$ elementary plaquettes. The basis states corresponding to such a junction is shown in the left panel of Fig. 15. The Hilbert space, as can be seen from this figure, is four dimensional. The tree for the states in the Hilbert space is shown in the bottom of the left panel Fig. 15. A straightforward analysis shows that H admits a four-dimensional matrix representation in the space of these states which can be written in terms of outer product of two sets of Pauli and

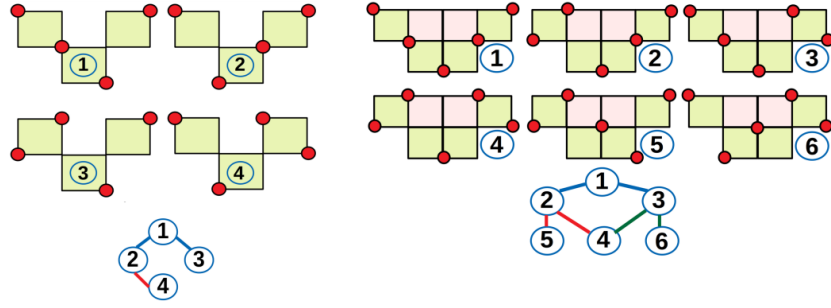


Figure 15: Left Panel:(a) Schematic representation of the basis states of the quantum drum corresponding to a junction of two wires as shown in Fig. 5 (A) with $N_p = 3$ and (b) the corresponding tree between the four states in the Hilbert space. Right Panel: Same as the left panel but corresponding to the simplest quantum drum (with $N_p = 4$) that can be treated as the junction unit to generate another junction of two wires as shown in Fig. 5 (B). In all plots, the red filled dots indicates sites with up-spins (bosons). The green (pink) plaquettes in the drums follow the same convention as used in Fig. 1.

identity matrices ($\vec{\tau}_a$ and I_a for $a = 1, 2$) as

$$H_{1j} = \tau_1^x \otimes (I_2 + \tau_2^z)/2 + I_1 \otimes \tau_1^x \quad (22)$$

The corresponding eigenvalues satisfy the characteristic equation $E^4 - 3E^2 + 1 = 0$ and yields a solution $E = \pm(1 \pm \sqrt{5})/2$. These eigenvalues therefore yield the golden ratio for this particular drum.

Next, we consider the simplest quantum drum that can be treated as the junction unit to generate another junction of two wires as shown in Fig. 5 (B). This unit corresponds to a drum with $N_p = 4$ as shown in the right panel of Fig. 15. The basis states spanning the six-dimensional Hilbert space is shown in the top of the right panel of Fig. 15 while the tree for these states is shown in the bottom of this figure. We find that the Hamiltonian has a 6×6 matrix representation given by

$$H_{3\ell} = \begin{pmatrix} 0 & 1 & 1 & 0 & 0 & 0 \\ 1 & 0 & 0 & 1 & 1 & 0 \\ 1 & 0 & 0 & 1 & 0 & 1 \\ 0 & 1 & 1 & 0 & 0 & 0 \\ 0 & 1 & 0 & 0 & 0 & 0 \\ 0 & 0 & 1 & 0 & 0 & 0 \end{pmatrix} \quad (23)$$

The characteristics equation for the eigenvalues simplifies to $E^2(E^2 - 1)(E^2 - 5) = 0$ and yields eigenvalues $E = 0$ (doubly degenerate) and $E = \pm 1, \pm\sqrt{5}$.

Next, we consider the simplest quantum drum that can be viewed as the junction unit of the junction of three wires shown in Fig. 5 (C). This drum has $N_p = 10$ plaquettes in it. The basis states spanning the Hilbert space is shown in the left panel of Fig. 16. The Hilbert space is 13 dimensional; the tree for these states is shown in the right panel of Fig. 16. This allows a 13×13 dimensional matrix representation of H . We do not write this matrix explicitly here since it can be easily constructed from the tree shown in Fig. 16. This matrix needs to be numerically

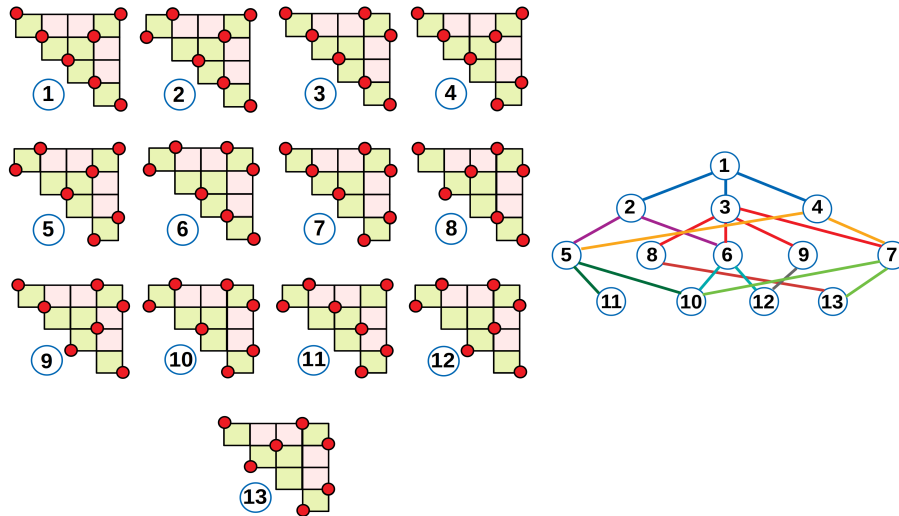


Figure 16: Left Panel: Schematic representation of the basis states of the simplest quantum drum that can be viewed as the junction unit of the junction of three wires shown in Fig. 5 (C) with $N_p = 10$ plaquettes. The red filled circles indicates sites with up-spins (bosons). Right Panel: The corresponding tree between the 13 states in the Hilbert space. The green (pink) plaquettes in the drum follows the same convention as used in Fig. 1.

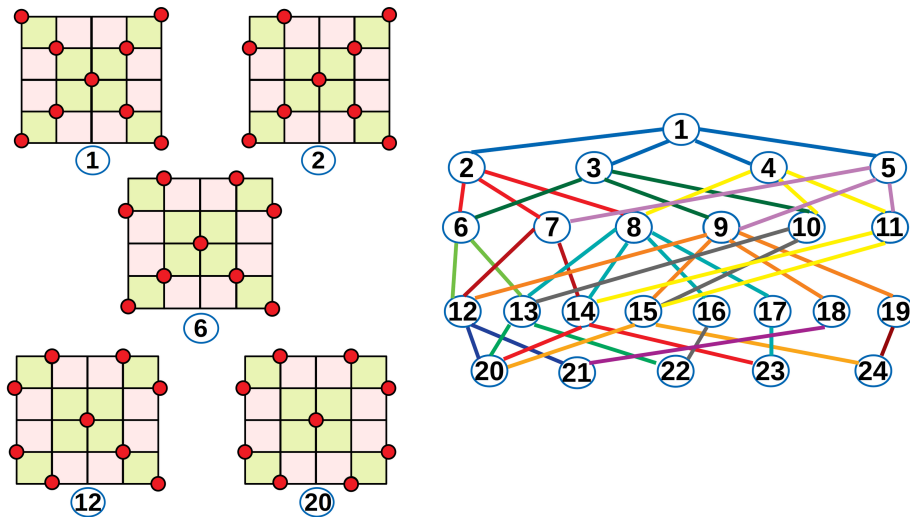


Figure 17: Left Panel: Schematic representation of a few basis states of the drum that can be viewed as the junction unit of a junction of four wires as shown in Fig. 5 (D). The drum contains $N_p = 16$ plaquettes. The red filled circles indicates sites with up-spins (bosons). Right Panel: The corresponding tree between the 24 states in the Hilbert space. Each of the states can be obtained from a state connected to it by application of H on it. The green (pink) plaquettes in the drum follows the same convention as used in Fig. 1. See text for details

diagonalized and yields eigenvalues $E = \pm 3.18259\dots, \pm 1.91182\dots, \pm(1 \pm \sqrt{5})/2, \pm 1, 0,$ and $\pm 0.464856\dots$.

Finally, we study a quantum drum that is the junction unit of a junction of four wires as shown in Fig. 5 (D). This junction unit is shown in Fig. 17 and corresponds to $N_p = 16$ with nine up-spins (bosons) and 24 basis states. A few representative such states are shown in the left panel of Fig. 17. Each of these states belong to a different level in the tree starting from the state $|1\rangle$ as shown in the right panel of Fig. 17; they can be obtained from the state in the preceding level shown by application of H . The other states can be analogously obtained following the tree; we do not show them explicitly to avoid clutter. The tree shows that H admits a 24×24 matrix representation. Remarkably, this matrix can be analytically diagonalized; its eigenvalues satisfies the characteristics equation

$$E^6(E^2 - 2E - 2)(E^2 - 2)(E^4 - 22E^2 + 80)(E^4 - 6E^2 + 6)^2(E^2 + 2E - 2) = 0 \quad (24)$$

These leads to the 24 eigenvalues given by 0 (six fold degenerate), $\pm\sqrt{3 \pm \sqrt{3}}$ (each two fold degenerate), $\pm\sqrt{11 \pm \sqrt{41}}, \pm\sqrt{2},$ and $\pm 1 \pm \sqrt{3}$.

5 Numerical study of large quantum drums

In this section, we will numerically calculate the spectrum of large quantum drums with N_p elementary plaquettes using the examples of a wire (Fig. 18, left and middle panels have $N_p = 4$ and 5, respectively) and a particular junction of two equal length wires (Fig. 18, right panel with $N_p = 7$). We refer to this latter case as “junction of two wires” henceforth. Using exact diagonalization (ED), we could calculate the spectrum up to $N_p = 22$ for the wire and $N_p = 23$ for the junction of two wires. We will show that the spectrum of a wire with N_p plaquettes is identical to the paradigmatic 1D PXP chain [12, 13] with N_p sites on a chain with OBC. This equivalence allows us to extract several features of the high-energy spectrum of the wire from known results in the literature [12, 13]. However, our numerical studies also reveal enhanced fidelity revivals from a period-3 initial state for $N_p = 3n + 1$, where n is an integer, without the need of adding any optimal perturbations to the Hamiltonian which was not pointed out earlier in the literature. While the junction of two wires differs from the wire by only a “surface term” when N_p is large, the structure of the Hilbert space is completely different and gives a different constrained model compared to the 1D PXP chain. Thus, the presence or absence of a single junction leads to interesting differences in the high-energy spectrum that persist for large drums.

5.1 Tree generating algorithm and equivalence of wire to 1D PXP chain

The concept of a unidirectional tree starting from a reference state has already been introduced in Sec. 4.1. The reference state for a wire with N_p plaquettes can be taken to be the Fock state with all $N_p + 1$ up-spins to be along the wire length as previously done in Sec. 3.2. For the junction of two wires with $N_p = 2x + 1$ plaquettes, we take the reference state to be the one where $x + 2$ $[x]$ up-spins (bosons) are arranged along the length of the wire of length $x + 1$ $[x]$ to the right $[left]$ of the central junction plaquette, including $[excluding]$ the junction plaquette (e.g., see an example of the reference state marked as ① in the left panel of Fig. 20.). For both the wire and the junction of two wires, computationally it is convenient to adopt a one-to-one map from a spin configuration on the wire or a junction of two wires to another defined on an open chain with

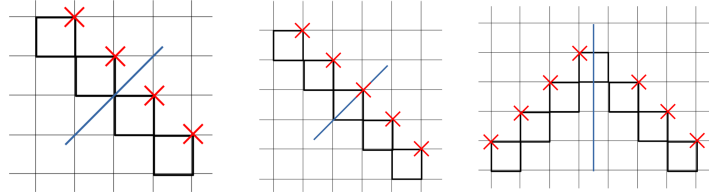


Figure 18: Two wires with $N_p = 4$ (left panel) and $N_p = 5$ (middle panel) respectively and a junction of two wires with $N_p = 7$ (right panel) are illustrated here. These quantum drums have a discrete reflection symmetry with the thick blue line in all the three panels indicating the corresponding axis of reflection.

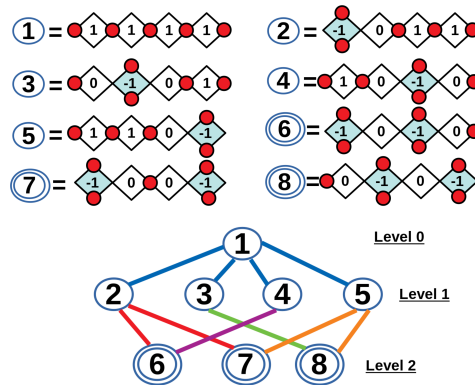


Figure 19: Tree structure (bottom panel) for a wire with $N_p = 4$ shown here. The i th level contains Fock states with i flipped plaquettes (indicated by shaded plaquettes in the top panel) with respect to the reference state defined in level-0. The nodes between two Fock states imply that these are connected with a single application of H . The Fock states enclosed by double circles represent dead ends of the tree. The corresponding value of the pseudospin variable ($\pm 1, 0$) is also shown at the center of each plaquette for each of the Fock states in the top panel.

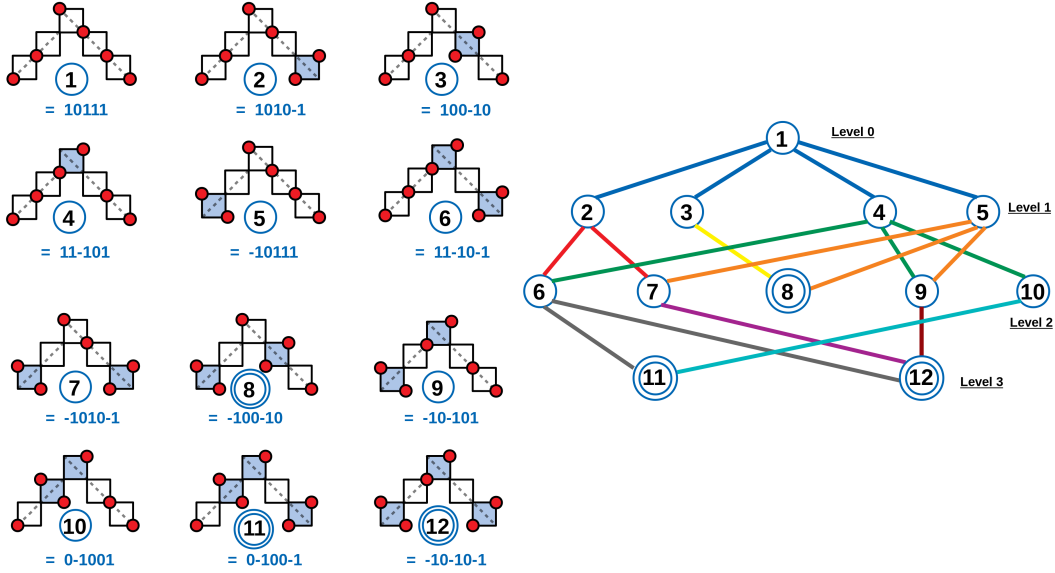


Figure 20: Tree structure for a junction of two wires with $N_p = 5$ shown here. The i th level contains Fock states with i flipped plaquettes (indicated by shaded plaquettes) with respect to the reference state defined in level-0. The nodes between two Fock states (where the links imply the forward construction of the tree) imply that these are connected with a single application of H . The Fock states enclosed by double blue circles represent dead ends of the tree. The pseudospins on an open chain with $N_p = 5$ sites is also shown for each of the Fock states in the left panel where red filled circles denote up-spins (bosons).

N_p sites in 1D where each site of the chain can have a pseudospin variable $\tau_i^z = \pm 1$ or 0, where $i = 1$ to N_p . The pseudospins on the chain represent the plaquettes of the drum sequentially from left to right in both the cases. For the wire, these variables take the value $+1$ (-1) for elementary plaquettes that have two up-spins along (perpendicular to) the wire direction and 0 otherwise (Fig. 19, top panel). For the junction of two wires, we follow the same convention and remove the ambiguity at the central plaquette by associating it to the wire to the right of the junction plaquette (Fig. 20, left panel). While a pseudospin with 0 has multiple possibilities associated with an elementary plaquette involving states with zero or one up-spin, specifying the locations of the ± 1 pseudospins also fixes the spin state of the other plaquettes on the drum.

The tree generating algorithm then proceeds as follows. One starts with the reference state which has τ_i^z equal to $111 \cdots 1$ for the wire and $11 \cdots 1011 \cdots 1$ for the junction of two wires where the 0 in the latter case represents the plaquette to the immediate left of the 1-junction plaquette. For the wire, the states at subsequent levels are generated by flipping a 1 to -1 and replacing the pseudospins at neighboring site(s) of the flipped pseudospin by 0 (Fig. 19). For the junction of two wires, the rules are practically the same except at the 1-junction plaquette denoted by the site i_0 on the open chain. When 1 is flipped to -1 at i_0 , while the pseudospin at $i_0 + 1$ is replaced by 0 as usual, the pseudospin at $i_0 - 1$ is replaced by 0 if the pseudospin at $i_0 - 2$ equals -1 , else it is replaced by $+1$ (Fig. 20). Following this algorithm, we generate the tree and the corresponding H matrix for both the quantum drums being discussed here.

We now show that the wire with N_p plaquettes has the same spectrum as that of the 1D PXP chain with N_p sites and OBC, whose Hamiltonian is defined as follows:

$$H_{\text{PXP}} = \sum_{i=2}^{N_p-1} P_{i-1} \mu_i^x P_{i+1} + \mu_1^x P_2 + P_{N_p-1} \mu_{N_p}^x \quad (25)$$

where μ_i^α for $\alpha = x, y, z$ represents spin-1/2 Pauli matrices at site i of the open chain with N_p sites, and $P_i = (1 - \mu_i^z)/2$ is a local projection operator. The constrained Hilbert space of the PXP chain is defined by the condition that no two nearest neighbor sites $i, i+1$ can have $\mu_i^z = +1$ and $\mu_{i+1}^z = +1$ together. We now make the following correspondence between the pseudospins τ_i^z for the wire and the spins μ_i^z for the PXP chain:

$$\begin{aligned} \tau_i^z = -1 &\Rightarrow \mu_i^z = +1, \\ \tau_i^z = +1 &\Rightarrow \mu_i^z = -1_f, \\ \tau_i^z = 0 &\Rightarrow \mu_i^z = -1_{\text{uf}} \end{aligned} \quad (26)$$

where $\mu_i^z = -1_f$ (-1_{uf}) implies that flipping μ_i^z from -1 to $+1$ is allowed (disallowed) due to the hard-core constraints of the PXP model. In this language, the reference state of the wire with $\tau_i^z = +1$ for all i corresponds to the ‘‘Rydberg vacuum’’ state of the PXP chain with no Rydberg excitations, i.e., $\mu_i^z = -1_f$ for all i . The tree generating algorithm then constructs a unidirectional tree starting from the reference state at level-0 by flipping a $\tau_i^z = 1$ to $\tau_i^z = -1$ and replacing the pseudospins at neighboring site(s) of the flipped pseudospin by $\tau_{i+1}^z = \tau_{i-1}^z = 0$ for $i \neq 1, N_p$ and $\tau_{i+1}^z = 0$ ($\tau_{i-1}^z = 0$) for $i = 1$ ($i = N_p$) at each subsequent level of the tree. The action of H_{PXP} in Fock space can also be represented by the same tree structure as the wire using Eq. 26 since flipping any μ_i from -1 to $+1$ starting from the Rydberg vacuum state automatically makes the previously flippable nearest neighbor site(s) with $\mu = -1$ unflippable due to the hard-core constraints of the PXP chain.

We note that this equivalence immediately breaks down for the junction of two wires since flipping a pseudospin $\tau_{i_0}^z = +1$ to $\tau_{i_0}^z = -1$ on the central junction plaquette, denoted by i_0 , starting from the reference state produces a flippable $\tau_{i_0-1}^z = +1$ to its immediate left (see Fock states marked by 1 and 4 in the left panel of Fig. 20 for an example) which implies that the junction of two wires cannot be represented by the same constrained Hilbert space as the PXP model by this mapping.

5.2 Hilbert space dimension and level statistics

Let us calculate the Hilbert space dimension for both these drums for an arbitrary N_p which will justify their interpretation as effective quasi-1D models since the dimensionality scales exponentially with N_p as $N_p \gg 1$ in both cases. Let us denote the number of possible Fock states for a wire with N_p plaquettes to be $\mathcal{N}_w(N_p)$. All the Fock states for such a wire can be built in either one of the following two ways. Consider starting from the reference state (Fig. 19, level-0 state) and building all possible Fock states using the first $N_p - 1$ plaquettes starting from the top. The number of generated states then equals $\mathcal{N}_w(N_p - 1)$ and it is easy to see that the last plaquette will then either have the pseudospin to be $+1$ or 0 . The remaining states of the wire with N_p plaquettes can be generated by starting from the reference state and fixing the pseudospin of the last plaquette to be -1 (i.e., flipping this last plaquette). The first $N_p - 2$ plaquettes from the top can then be

used to generate the missing Fock states whose number equals $\mathcal{N}_w(N_p - 2)$. Thus, we get that

$$\begin{aligned}\mathcal{N}_w(N_p) &= \mathcal{N}_w(N_p - 1) + \mathcal{N}_w(N_p - 2) \\ &= F_{N_p+2}\end{aligned}\quad (27)$$

By construction, $\mathcal{N}_w(1) = 2$ and $\mathcal{N}_w(2) = 3$ which implies that $\mathcal{N}_w(N_p) = F_{N_p+2}$ as written above, where F_n are the Fibonacci numbers defined by the recurrence relation $F_0 = 0$, $F_1 = 1$ and $F_n = F_{n-1} + F_{n-2}$ for $n > 1$.

Similarly, for the junction of two wires with $N_p = 2x + 1$ plaquettes, all the Fock states can again be built in one of the following two ways. Consider starting from the reference state (Fig. 20, level-0 state) and building all possible Fock states of the left wire with $x - 1$ plaquettes starting from the left-bottom plaquette and the right wire with $x + 1$ plaquettes starting from the right-bottom plaquette. The number of such states equal $\mathcal{N}_w(x - 1)\mathcal{N}_w(x + 1)$ and the plaquette to the immediate left of the central junction plaquette can have a pseudospin of either be $+1$ or 0 . To generate the remaining configurations, we start from the reference state again and make the pseudospin of this particular plaquette to be -1 by first flipping the central junction plaquette and then flipping the plaquette to the immediate left of the junction. The number of Fock states generated from the rest of the plaquettes then equals $\mathcal{N}_w(x - 1)\mathcal{N}_w(x - 2)$, thus giving the relation

$$\mathcal{N}_j(N_p = 2x + 1) = \mathcal{N}_w(x - 1)[\mathcal{N}_w(x - 2) + \mathcal{N}_w(x + 1)] = F_{x+1}(F_x + F_{x+3}) \quad (28)$$

where $\mathcal{N}_j(N_p = 2x + 1)$ refers to the number of Fock states in a junction of two wires composed of $N_p = 2x + 1$ elementary plaquettes. Eq. 27 and Eq. 28 show that the number of allowed Fock states scale exponentially for large N_p for both the drums. Note that while Eq. 27 is identical to the Hilbert space dimension of a 1D PXP chain with N_p sites and OBC, as should be the case from the equivalence of both models shown in Sec. 5.1, the Hilbert space dimension of the junction of two wires (Eq. 28) cannot be expressed as F_m with an integer m in general showing that the structure of the constrained Hilbert space of this drum is different from that of the 1D PXP chain.

We can then ask whether these large quantum drums satisfy a Krylov-restricted version of the ETH, i.e., whether these quasi-1D models are non-integrable. We check this using the method of level statistics that can be obtained directly using the eigenspectrum from ED (e.g., see Ref. [76]). To calculate the level statistics for large quantum drums, it is important to first project to a sector where all the commuting global symmetries have been resolved. Since both the wire and the junction of two wires (Fig. 18) are quasi-1D structures with open boundaries, momentum is not a good quantum number. The total magnetization in the computational basis, S_{tot}^z , represents a conserved quantity for these drums. However, all nodes of a tree (Fig. 19 and Fig. 20) already have the same S_{tot}^z by construction. The only remaining non-trivial global symmetry turns out to be a reflection symmetry, denoted by \mathcal{R}_w (\mathcal{R}_j) for the wire (junction of two wires), which takes a Fock state $|\alpha\rangle$ to another Fock state $|\beta\rangle = \mathcal{R}_{w/j}|\alpha\rangle$ with the axis of reflection shown in Fig. 18 for both the drums. For a wire with even (odd) number of plaquettes, the axis passes through a site (the diagonal of a square) (Fig. 18, left and middle panels) whereas for a junction of two wires, it passes through the central junction plaquette as shown in Fig. 18, right panel. Since $\mathcal{R}_{w/j}^2|\alpha\rangle = |\alpha\rangle$ for any Fock state, the basis states $(|\alpha\rangle \pm \mathcal{R}_{w/j}|\alpha\rangle)/\sqrt{2}$ define states with $\mathcal{R}_{w/j} = \pm 1$ respectively. If $\mathcal{R}_{w/j}|\alpha\rangle = |\alpha\rangle$ for some Fock state(s), then such Fock state(s) only contribute to the $\mathcal{R}_{w/j} = +1$ sector. This happens in the case of the wire, where, the reference state provides one example of such a Fock state. Thus, the number of basis states in $\mathcal{R}_w = +1$ always exceeds the corresponding number for $\mathcal{R}_w = -1$ for a wire whereas these two numbers are equal to each other for a junction of two wires.

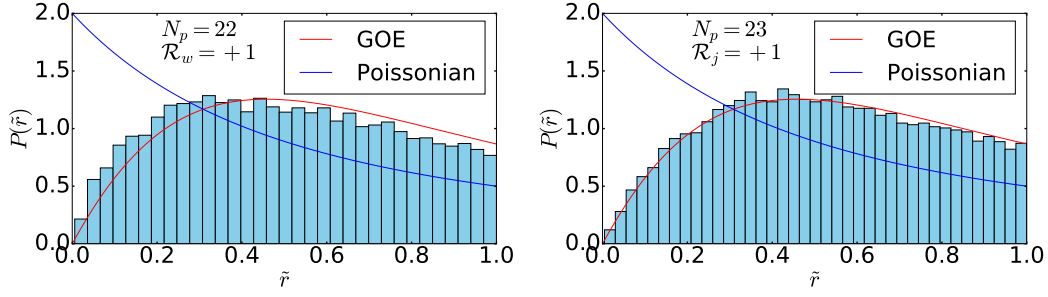


Figure 21: Level spacing ratio distribution $P(\tilde{r})$ versus \tilde{r} for a wire with $N_p = 22$ (left panel) and a junction of two wires with $N_p = 23$ (right panel), with both the data taken in the symmetry sector with $\mathcal{R}_{w/j} = +1$. The histograms indicate the non-integrability of both the quasi-1D models.

Restricting to the larger sector with $\mathcal{R}_{w/j} = +1$, we construct the distribution of consecutive level spacing ratios \tilde{r} (with support in $[0, 1]$) where \tilde{r} is defined as follows:

$$\tilde{r} = \min \left\{ r_n, \frac{1}{r_n} \right\} \leq 1, \quad r_n = \frac{s_n}{s_{n-1}}, \quad s_n = E_{n+1} - E_n \quad (29)$$

where E_n represent the energies of the eigenvectors obtained from ED. For a non-integrable model, one expects a Gaussian orthogonal ensemble (GOE) distribution, while an integrable system leads to a Poisson distribution for $P(\tilde{r})$ [77], where the two distributions have the following forms:

$$P_{\text{GOE}}(\tilde{r}) = \frac{27}{4} \frac{\tilde{r} + \tilde{r}^2}{(1 + \tilde{r} + \tilde{r}^2)^{5/2}}; \quad P_{\text{P}}(\tilde{r}) = \frac{2}{(1 + \tilde{r})^2}. \quad (30)$$

The numerically generated data for $P(\tilde{r})$ versus \tilde{r} is shown for a wire with $N_p = 22$ plaquettes and a junction of two wires with $N_p = 23$ plaquettes in Fig. 21. The data clearly indicates that $P(\tilde{r})$ follows $P_{\text{GOE}}(\tilde{r})$ much more closely than $P_{\text{P}}(\tilde{r})$ for these system sizes giving strong evidence for the non-integrable nature of both these quasi-1D models.

5.3 Zero modes and index theorem

While both the wire and the junction of two wires have a symmetric eigenspectrum of H around $E = 0$ as is expected for any quantum drum, the ED data further reveals the presence of an ever-increasing number of exact zero modes (up to machine precision) with increasing N_p for the former case and the absence of any zero mode for the latter case.

This striking difference between the two drums can be understood in terms of the index theorem of Ref. [73]. Firstly, a chiral operator $C_{w/j} = \prod_{\square_j} \sigma_{j_x, j_y}^z$ (where the subscript $w(j)$ refers to the wire (junction of two wires)) can be defined in both cases, which involves one site (j_x, j_y) per elementary plaquette contained in the drum (these sites are indicated by crosses in red in all panels of Fig. 18). This operator satisfies $\{H, C_{w/j}\} = 0$ for the Hilbert space fragments generated by these drums, thus ensuring the $E \rightarrow -E$ symmetry of the spectrum. Furthermore, as already discussed, these two drums have a global reflection symmetry, $\mathcal{R}_{w/j}$, that commutes with H (Fig. 18). Importantly, while $[\mathcal{R}_w, C_w] = 0$, it turns out that $[\mathcal{R}_j, C_j] \neq 0$ which means that the index theorem of Ref. [73] applies to the wire but not to junction of two wires. This leads to a

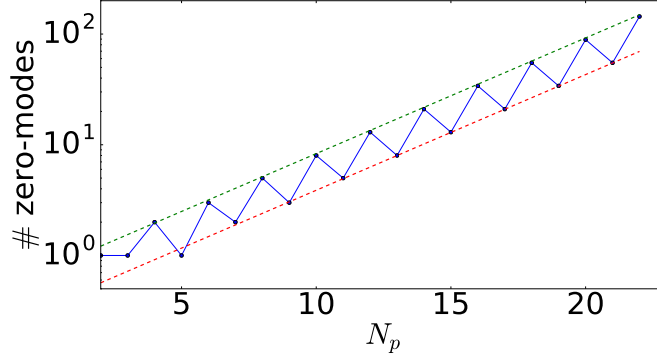


Figure 22: Scaling of the total number of zero modes versus N_p for a wire. For even (odd) values of N_p , the number of zero modes grow as $\mu_e(\sqrt{\varphi})^{N_p}$ ($\mu_o(\sqrt{\varphi})^{N_p}$) where $\mu_e \approx 0.75$ ($\mu_o \approx 0.35$) [indicated by dotted lines].

macroscopically large number of protected zero modes in the former case and also explains our numerical data (Fig. 22). The number of zero modes in the wire show an interesting even-odd effect as a function of N_p (Fig. 22) with the even values of N_p showing a higher number of zero modes. This even-odd effect stems from the fact that the axis that defines the reflection symmetry, \mathcal{R}_w , passes through a single site shared by two elementary plaquettes for even values of N_p ; in contrast, it passes through two sites along a diagonal of an elementary plaquette for odd values of N_p (Fig. 18, left and middle panels). The number of zero modes scale as $\mu_{e/o}(\sqrt{\varphi})^{N_p}$ (with $\varphi = (1 + \sqrt{5})/2$ being the golden ratio as defined before) where $\mu_e \approx 0.75$ ($\mu_o \approx 0.35$) for even (odd) values of N_p (see Fig. 22). Identical scaling behavior was also observed for the number of zero modes in the 1D PXP model [12, 13, 78].

It is useful to point out here that a different type of junction of two equal-length wires (Fig. 5, panel B) instead of this junction being studied here will again have an exponentially large number of exact zero modes. Similarly, a junction of three equal-length wires (Fig. 5, panel C) as well as a junction of four equal-length wires (Fig. 5, panel D) will also have a macroscopic number of zero modes due to the index theorem of Ref. [73]. It is interesting to see how the number of zero modes scales as a function of N_p for these quasi-1D cases as $N_p \gg 1$.

5.4 QMBS and related diagnostics

While the level statistics distribution of both the wire and the junction of two wires (Fig. 21) is consistent with these quasi-1D models being non-integrable for large N_p and thus satisfying Krylov-restricted ETH, both quantum drums also harbor QMBS that give rise to observable dynamical signatures like periodic revivals from certain simple initial states.

Let us consider three such Fock states for the wire as shown in Fig. 23. Fig. 23 (left panel) shows the reference state which we denote as $|r\rangle_w$, Fig. 23 (middle panel) shows a Fock state obtained by flipping every alternate elementary plaquette in the reference state which we denote as $|fu\rangle_w$, and Fig. 23 (right panel) shows a Fock state obtained by flipping every third elementary plaquette in the reference state which we denote as $|fuu\rangle_w$. Similarly, two representative Fock states are shown in Fig. 24 for the junction of two wires. Fig. 24 (left panel) shows the reference state which we denote as $|r\rangle_j$ (note that there are two such reference states possible for the junction

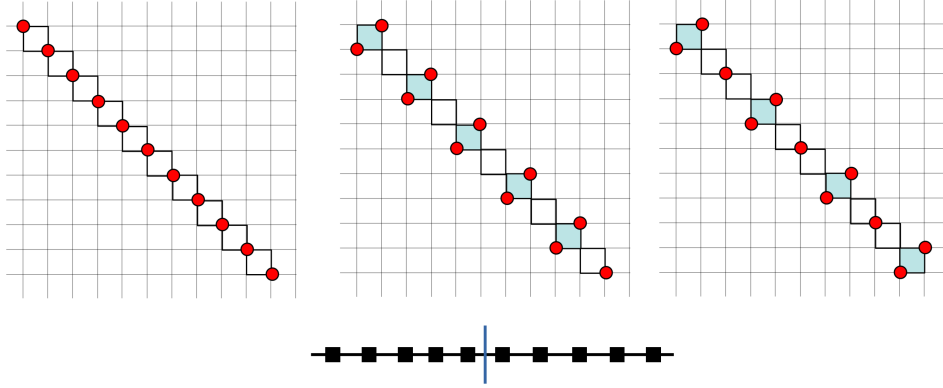


Figure 23: Three Fock states shown for the wire with $N_p = 10$. (Left panel) Reference state denoted by $|r\rangle_w$ (Middle panel) A $|fu\rangle_w$ state created by flipping every alternate elementary plaquette in the reference state (Right panel) A $|fuu\rangle_w$ state created by flipping every third elementary plaquette of the reference state. Flipped plaquettes with respect to the reference state are shown shaded in blue. The entanglement cut used to calculate the bipartite entanglement entropy of the system after mapping it to an open chain of pseudospins is shown below; such a cut divides the system into two equal halves with $N_p/2$ pseudospins each.

of two wires) and Fig. 24 (right panel) shows a Fock state obtained by flipping every alternate elementary plaquette in the reference state which we denote as $|fu\rangle_j$. From the equivalence of the wire to the 1D PXP chain shown in Sec. 5.1, it is clear that while local operators starting from the state $|r\rangle_w$ will thermalize quickly, since the initial state maps to the Rydberg vacuum state of the PXP chain, this will not be the case from the initial states $|fu\rangle_w$ and $|fuu\rangle_w$ which map to the period-2 $|\mathbb{Z}_2\rangle$ and the period-3 $|\mathbb{Z}_3\rangle$ Fock states of the PXP chain, respectively.

This can indeed be checked by monitoring the fidelity $F(t) = |\langle s | \exp(-iHt) | s \rangle|^2$ using ED for these representative Fock states (denoted by $|s\rangle$) in Fig. 25. Most initial states show a rapid drop in $F(t)$ within $t \sim O(1)$ which is expected for a high-energy initial state in an interacting system. However, for the wire, the behaviour of $F(t)$ for $|fu\rangle_w$ and $|fuu\rangle_w$ are markedly different, with both showing periodic revivals with an emergent time-scale $T^* \sim 5$ for $|fu\rangle_w$ (Fig. 25, top-left panel) and $T^* \sim 4$ for $|fuu\rangle_w$ (Fig. 25, top-right panel). The periodic revivals of $F(t)$ starting from $|fu\rangle_w$ show a decaying envelope in time that can be reasonably described by the envelope function $\exp(-t/\tau_w)$ with $\tau_w \approx 10$ (Fig. 25, top-left panel). This decaying envelope to the periodic revivals distinguish this phenomenon from the persistent oscillations starting from initial Fock states discussed in Sec. 2.3. In fact, the fidelity revivals for the $|fuu\rangle_w$ state shows a very interesting finite-size effect with such revivals being strongest when $N_p = 3n + 1$ where n is an integer. For example, the peak value of the first fidelity revival in time equals 0.52 for $N_p = 19$ while it is much smaller for $N_p = 18$ and $N_p = 20$ (0.22 and 0.18 respectively). Furthermore, the $N_p = 19$ data for $F(t)$ starting from the initial state $|fuu\rangle_w$ shows no sign of a decaying exponential envelope till $t = 50$ (see Fig. 25, top-right panel). For the junction of two wires with $N_p = 23$, we again see rapid decay of $F(t)$ starting from $|r\rangle_j$ (Fig. 25, bottom-left panel) while $F(t)$ shows non-trivial periodic revivals from $|fu\rangle_j$ with the same $T^* \sim 5$ as in the wire case. The periodic revivals are weaker for the junction of two wires compared to the single wire and again have a decaying exponential envelope described by $\exp(-t/\tau_j)$ with a smaller $\tau_j \approx 7$, but these fidelity revivals

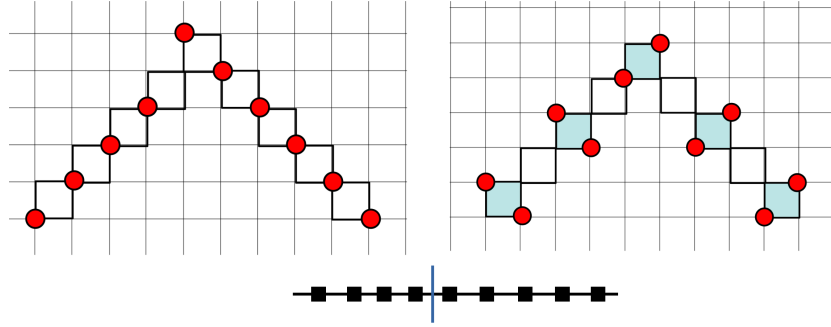


Figure 24: Two Fock states shown for the junction of two wires with $N_p = 9$. (Left panel) Reference state denoted by $|r\rangle_j$ (Right panel) A $|f u\rangle_j$ state created by flipping every alternate elementary plaquette in the reference state. Flipped plaquettes with respect to the reference state are shown shaded in blue. The entanglement cut used to calculate the bipartite entanglement entropy of the system after mapping it to an open chain of pseudospins divides the system into two halves with $(N_p/2) \pm 1$ pseudospins as shown below.

are nonetheless clearly visible up to $t \sim 20$.

It is useful to point out that the enhanced revivals observed for $|f u u\rangle_w$ for $N_p = 3n + 1$ for the wire, which is equivalent to a $|\mathbb{Z}_3\rangle$ initial state in a 1D PXP chain with N_p sites and OBC, was not pointed out in the literature previously and additional terms were added to the PXP Hamiltonian to cause enhancement of fidelity revivals from the $|\mathbb{Z}_3\rangle$ state [79]. As is well-known from the 1D PXP chain [12, 13], these fidelity revivals from certain special initial states is due to a large overlap with *approximate* towers of QMBS that are equally spaced in energy. These towers are most clearly seen by plotting the overlaps of the initial Fock state $|f u u\rangle_w$ with the many-body eigenstates $|E\rangle$ as a function of energy (see Fig. 26). We see that at $N_p = 3n + 1$ (Fig. 26, middle panel), these towers are much more clearly formed compared to $N_p = 3n$ (Fig. 26, left panel) and to $N_p = 3n + 2$ (Fig. 26, right panel). We also note that at the system sizes, $N_p = 3n + 1$, the $|f u u\rangle_w$ Fock state becomes orthogonal to the zero mode subspace of the system (up to machine precision) even though the initial state has zero average energy. A deeper understanding of all these striking finite-size effects at $N_p = 3n + 1$ for the wire/open PXP chain would be highly desirable.

Even though the junction of two wires cannot be reduced to the 1D PXP chain, this model also admit *approximate* towers of QMBS that are equidistant in energy. In Fig. 27 (two panels), the overlap behavior of the $|f u\rangle_j$ Fock state (Fig. 24, right panel) with the eigenstates of the junction of two wires with $N_p = 23$ is shown for the $\mathcal{R}_j = +1$ and the $\mathcal{R}_j = -1$ sectors respectively. In this case, the towers of states with higher overlap to the Fock state are somewhat less clearly separated from the bulk of the spectrum as compared to the 1D PXP model, explaining the weaker fidelity revivals in the junction of two wires as compared to the single wire case (Fig. 25, top left and bottom right panels). Since $[\mathcal{R}_j, \mathcal{C}_j] \neq 0$, the overlaps are not symmetric with respect to zero energy; rather, the overlap behavior for $\mathcal{R}_j = +1$ sector is a *mirror image* (with the mirror axis being $E = 0$) of the $\mathcal{R}_j = -1$ sector.

Another tell-tale signature for the presence of QMBS is that such states have anomalously low bipartite entanglement entropy compared to neighboring eigenstates with similar energies. The

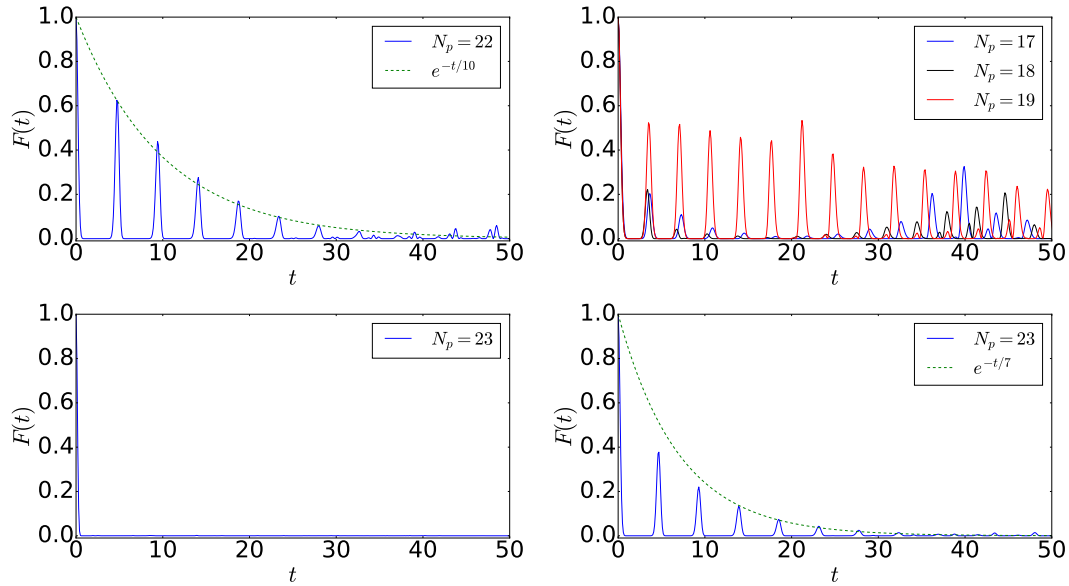


Figure 25: The behavior of fidelity $F(t)$ shown for the wire with two different initial Fock states with the top-left panel for $|fu\rangle_w$, and the the top-right panel for $|fuu\rangle_w$. The bottom-left (bottom-right) panel shows the fidelity as a function of time with the initial state being $|r\rangle_j$ ($|fu\rangle_j$) for a junction of two wires.

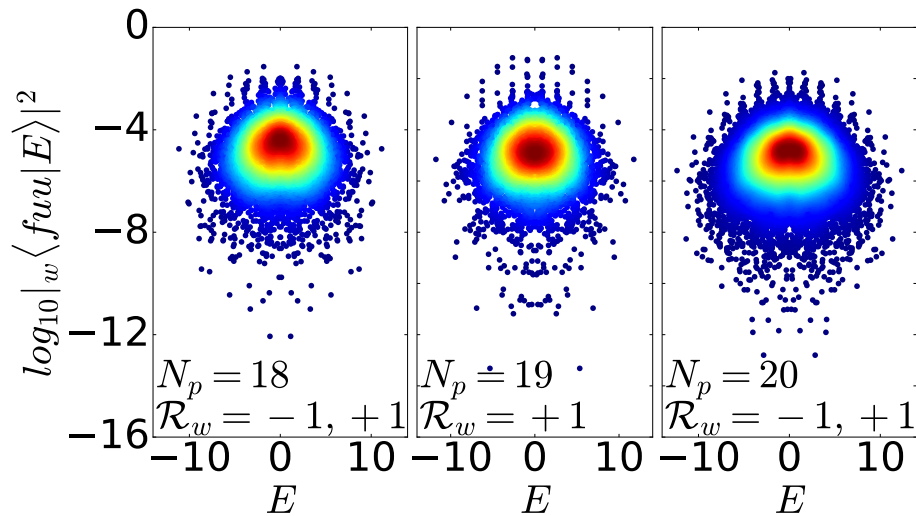


Figure 26: Density plots showing the overlap of the $|fuu\rangle_w$ state with energy eigenstates of the wire with $N_p = 18$ (left panel), $N_p = 19$ (middle panel) and $N_p = 20$ (right panel) respectively. In all the panels, the density of states is indicated by the same color map where warmer color corresponds to higher density of states.

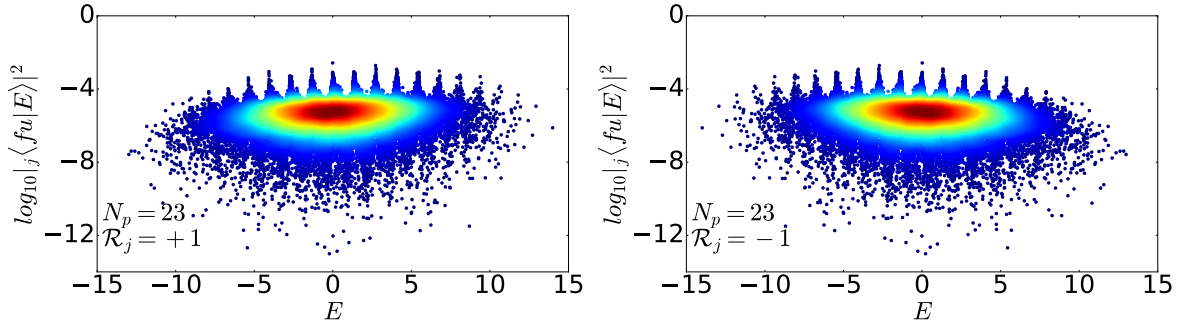


Figure 27: Density plots that show the overlap of the $|fu\rangle_j$ state for a junction of two wires with energy eigenstates of the junction with two wires with $N_p = 23$ for the $\mathcal{R}_j = +1$ (left panel) and the $\mathcal{R}_j = -1$ (right panel) sectors respectively. In both panels, the density of states is indicated by the same color map where warmer color corresponds to higher density of states.

bipartite entanglement entropy is given by

$$S(A) = -\text{Tr}[\rho_A \ln \rho_A] \quad (31)$$

for each eigenstate $|\Psi\rangle$ where $\rho_A = \text{Tr}_{\bar{A}}|\Psi\rangle\langle\Psi|$ where ρ_A represents the reduced density matrix obtained by partitioning the system in to two spatial regions, A and its complement \bar{A} . We find it convenient to compute the bipartite entanglement entropy by adopting the one-to-one mapping of Fock states in a wire or a junction of two wires to pseudospins with values $0, \pm 1$ in a 1D open chain with N_p sites, with the mapping explained in Sec. 5.1. We then take \bar{A} to be the first $N_p/2$ sites of the 1D chain for the wire (as shown in Fig. 23) and the first $(N_p/2) - 1$ sites of the 1D chain for the junction of two wires (as shown in Fig. 24). The results of such a computation from ED are shown in Fig. 28 for the wire (top-left panel) and the junction of two wires (top-right panel) respectively. While both the panels show a presence of several anomalous eigenstates with lower bipartite entanglement entropy than the bulk of the spectrum, the wire shows a broader distribution of values especially in the neighborhood of $E = 0$ compared to the junction of two wires.

The expectation value of any local operator in a high-energy eigenstate is supposed to approach the thermal result, with the inverse temperature being fixed by the energy density of the eigenstate, for a system that satisfies ETH. In Fig. 28 (bottom panels), we consider the expectation value $\langle\Psi|\mathcal{O}|\Psi\rangle$ as a function of energy, where $|\Psi\rangle$ denotes an eigenstate of the wire (bottom left panel) or the junction of two wires (bottom right panel) and $\mathcal{O} = \sigma_1^z \sigma_3^z + \sigma_2^z \sigma_4^z$ where sites 1, 2, 3, 4 represent the four sites (in a clockwise manner) of the $N_p/2$ -th elementary plaquette from the top-left for a wire and the central junction plaquette for the junction of two wires. Since this local operator is located away from the edges of the system, it represents a bulk operator in both the cases. The thermal result as a function of energy is represented by dotted curves on both the lower panels of Fig. 28. While the expectation value of the local operator for the bulk of the spectrum indeed approaches the thermal result, several eigenstates do show an expectation value that is quite far from the corresponding thermal result. The wire again shows a much larger variation in the range of expectation values compared to the junction of two wires, especially in the vicinity of $E = 0$. Interestingly, the latter case shows tower-like structures that are equidistant in energy

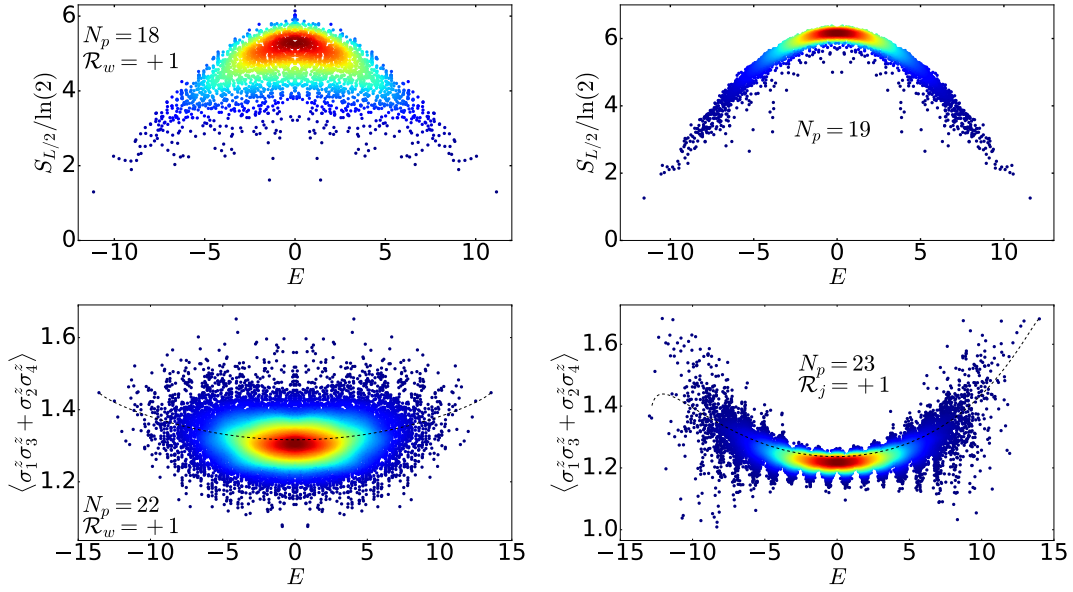


Figure 28: The behavior of the bipartite entanglement entropy for each eigenstate shown for (top left panel) a wire with $N_p = 18$ in the $\mathcal{R}_w = +1$ sector and for (top right panel) a junction of two wires with $N_p = 19$ for both $\mathcal{R}_j = \pm 1$ sectors together. The expectation value of a local diagonal operator defined on an elementary plaquette for each energy eigenstate shown for the wire with $N_p = 22$ (bottom left panel) and the junction of two wires with $N_p = 23$ (bottom right panel) respectively, both in the symmetry sector $\mathcal{R}_{w/j} = +1$. The dotted lines in both the lower panels indicate the thermal values as a function of the energy E . In all the panels, the density of states is indicated by the same color map where warmer color corresponds to higher density of states.

(Fig. 28 (bottom right panel)) with a similar spacing between them as the tower of scar states visible in the overlap plots (Fig. 26, two panels).

6 Discussion

In conclusion, we have considered a spin-1/2 model on the two-dimensional square lattice in a constrained Hilbert space where no two nearest-neighbor sites can have up-spins simultaneously. The interaction Hamiltonian is composed of ring-exchange terms on elementary plaquettes that not only conserve the total magnetization but also the magnetization along each column and row of the square lattice. These additional subsystem symmetries imply conservation of a global dipole moment that leads to the phenomenon of Hilbert space fragmentation. While microscopic models of both weak and strong fragmentation are known in one dimension, we show that this particular interacting model with hard-core constraints presents a rare example of strong Hilbert space fragmentation in higher dimensions.

All the many-body eigenstates of this model can be expressed in terms of the tensor product of modes of appropriate quantum drums and any left-over inert spins. Given an initial unentangled product state in the computational basis, the associated quantum drums get fixed and come in a variety of shapes and sizes starting from one-plaquette drums to truly extensive structures made of plaquettes that share edges and/or vertices with each other. Specifying the plaquettes that belong to a drum uniquely fixes its spectrum. Crucially, these drums can be “shielded” from each other by shielding regions that only grow as the perimeter and not the area of such drums.

Large quantum drums and their associated fragment dimensions can be most easily estimated by using a “wire” decomposition of such drums and then counting the number of ways in which such wires can fluctuate simultaneously without violating the kinematic constraints. This allows us to identify the appropriate drums that dominate statistically for a given density of up-spins (bosons). It is shown that typical initial product states evade ETH-predicted thermalization due to the presence of either an extensive number of inert spins or an extensive number of next-nearest neighbor spin correlations that are pinned to their initial athermal values.

We consider the spectrum of some small drums analytically to show the emergence of interesting zero, non-zero integer and irrational modes. Close packing an extensive number of the elementary one-plaquette drums already generate many-body eigenstates with integer energies (including zero) and strict area-law scaling of entanglement entropy. Large quasi-one-dimensional and two-dimensional quantum drums can be viewed as interesting interacting systems with constrained Hilbert spaces. A class of these drums harbor a large number of exact zero modes. The simplest quasi-one-dimensional drum, which we dub as a wire, is shown to be exactly equivalent to the well-known PXP chain with open boundary conditions. However, a particular junction of two wires is also studied which cannot be mapped in to the PXP chain and represents a different constrained model. Both these quasi-one-dimensional drums support distinct families of quantum many-body scars that cause periodic revivals from certain simple initial states. Our numerics for the wire also shows that the period-3 state with Rydberg excitations on every third site shows strong revivals for open chains of length $3n + 1$ without the necessity of adding further perturbations to the PXP chain. This result can have possible implications for experiments with Rydberg atoms.

Several possible open directions emerge from our study. Other junctions of wires, like junctions of three wires and four wires, as well as some of the two-dimensional drums introduced

here should have interesting high-energy properties. It is further possible to add diagonal interactions in the computational basis which preserve the fragmented structure of the model. Using such additional interactions, one can possibly access different phases and phase transitions at zero temperature in both quasi-one-dimensional and two dimensional theories in the presence of subsystem symmetries.

Note added: While preparing this manuscript, we came to know of a related work by Lehmann *et al.* [80] which discusses strong Hilbert space fragmentation in higher dimensions using a different Hamiltonian (correlated hopping model).

Acknowledgements: K.S. thanks DST, India for support through SERB project JCB/2021/000030. AC thanks Madhumita Sarkar for help with cluster facilities and DST, India for support through SERB project PDF/2021/001134.

References

- [1] M. Rigol, V. Dunjko and M. Olshanii, *Thermalization and its mechanism for generic isolated quantum systems*, Nature **452**(7189), 854 (2008), doi:[10.1038/nature06838](https://doi.org/10.1038/nature06838).
- [2] J. M. Deutsch, *Quantum statistical mechanics in a closed system*, Phys. Rev. A **43**, 2046 (1991), doi:[10.1103/PhysRevA.43.2046](https://doi.org/10.1103/PhysRevA.43.2046).
- [3] M. Srednicki, *Chaos and quantum thermalization*, Phys. Rev. E **50**, 888 (1994), doi:[10.1103/PhysRevE.50.888](https://doi.org/10.1103/PhysRevE.50.888).
- [4] L. D'Alessio, Y. Kafri, A. Polkovnikov and M. Rigol, *From quantum chaos and eigenstate thermalization to statistical mechanics and thermodynamics*, Advances in Physics **65**(3), 239 (2016), doi:[10.1080/00018732.2016.1198134](https://doi.org/10.1080/00018732.2016.1198134), <https://doi.org/10.1080/00018732.2016.1198134>.
- [5] A. Dymarsky, N. Lashkari and H. Liu, *Subsystem eigenstate thermalization hypothesis*, Phys. Rev. E **97**, 012140 (2018), doi:[10.1103/PhysRevE.97.012140](https://doi.org/10.1103/PhysRevE.97.012140).
- [6] I. Bloch, *Ultracold quantum gases in optical lattices*, doi:[10.1038/nphys138](https://doi.org/10.1038/nphys138) (2005).
- [7] T. Langen, R. Geiger and J. Schmiedmayer, *Ultracold atoms out of equilibrium*, Annual Review of Condensed Matter Physics **6**(1), 201 (2015), doi:[10.1146/annurev-conmatphys-031214-014548](https://doi.org/10.1146/annurev-conmatphys-031214-014548), <https://doi.org/10.1146/annurev-conmatphys-031214-014548>.
- [8] J. G. Bohnet, B. C. Sawyer, J. W. Britton, M. L. Wall, A. M. Rey, M. Foss-Feig and J. J. Bollinger, *Quantum spin dynamics and entanglement generation with hundreds of trapped ions*, Science **352**(6291), 1297 (2016), doi:[10.1126/science.aad9958](https://doi.org/10.1126/science.aad9958), <https://www.science.org/doi/pdf/10.1126/science.aad9958>.
- [9] D. Bluvstein, A. Omran, H. Levine, A. Keesling, G. Semeghini, S. Ebadi, T. T. Wang, A. A. Michailidis, N. Maskara, W. W. Ho, S. Choi, M. Serbyn *et al.*, *Controlling quantum many-body dynamics in driven rydberg atom arrays*, Science **371**(6536), 1355 (2021), doi:[10.1126/science.abg2530](https://doi.org/10.1126/science.abg2530), <https://www.science.org/doi/pdf/10.1126/science.abg2530>.

- [10] M. Kjaergaard, M. E. Schwartz, J. Braumüller, P. Krantz, J. I.-J. Wang, S. Gustavsson and W. D. Oliver, *Superconducting qubits: Current state of play*, Annual Review of Condensed Matter Physics **11**(1), 369 (2020), doi:[10.1146/annurev-conmatphys-031119-050605](https://doi.org/10.1146/annurev-conmatphys-031119-050605), <https://doi.org/10.1146/annurev-conmatphys-031119-050605>.
- [11] H. Bernien, S. Schwartz, A. Keesling, H. Levine, A. Omran, H. Pichler, S. Choi, A. S. Zibrov, M. Endres, M. Greiner, V. Vuletić and M. D. Lukin, *Probing many-body dynamics on a 51-atom quantum simulator*, Nature **551**(7682), 579 (2017), doi:[10.1038/nature24622](https://doi.org/10.1038/nature24622).
- [12] C. J. Turner, A. A. Michailidis, D. A. Abanin, M. Serbyn and Z. Papić, *Weak ergodicity breaking from quantum many-body scars*, Nature Physics **14**(7), 745 (2018), doi:[10.1038/s41567-018-0137-5](https://doi.org/10.1038/s41567-018-0137-5).
- [13] C. J. Turner, A. A. Michailidis, D. A. Abanin, M. Serbyn and Z. Papić, *Quantum scarred eigenstates in a rydberg atom chain: Entanglement, breakdown of thermalization, and stability to perturbations*, Phys. Rev. B **98**, 155134 (2018), doi:[10.1103/PhysRevB.98.155134](https://doi.org/10.1103/PhysRevB.98.155134).
- [14] S. Sachdev, K. Sengupta and S. M. Girvin, *Mott insulators in strong electric fields*, Phys. Rev. B **66**, 075128 (2002), doi:[10.1103/PhysRevB.66.075128](https://doi.org/10.1103/PhysRevB.66.075128).
- [15] I. Lesanovsky and H. Katsura, *Interacting fibonacci anyons in a rydberg gas*, Phys. Rev. A **86**, 041601 (2012), doi:[10.1103/PhysRevA.86.041601](https://doi.org/10.1103/PhysRevA.86.041601).
- [16] J. Kogut and L. Susskind, *Hamiltonian formulation of wilson's lattice gauge theories*, Phys. Rev. D **11**, 395 (1975), doi:[10.1103/PhysRevD.11.395](https://doi.org/10.1103/PhysRevD.11.395).
- [17] J. B. Kogut, *An introduction to lattice gauge theory and spin systems*, Rev. Mod. Phys. **51**, 659 (1979), doi:[10.1103/RevModPhys.51.659](https://doi.org/10.1103/RevModPhys.51.659).
- [18] D. Horn, *Finite Matrix Models With Continuous Local Gauge Invariance*, Phys. Lett. B **100**, 149 (1981), doi:[10.1016/0370-2693\(81\)90763-2](https://doi.org/10.1016/0370-2693(81)90763-2).
- [19] P. Orland and D. Rohrlich, *Lattice Gauge Magnets: Local Isospin From Spin*, Nucl. Phys. B **338**, 647 (1990), doi:[10.1016/0550-3213\(90\)90646-U](https://doi.org/10.1016/0550-3213(90)90646-U).
- [20] S. Chandrasekharan and U.-J. Wiese, *Quantum link models: A discrete approach to gauge theories*, Nuclear Physics B **492**(1-2), 455 (1997).
- [21] A. Mil, T. V. Zache, A. Hegde, A. Xia, R. P. Bhatt, M. K. Oberthaler, P. Hauke, J. Berges and F. Jendrzejewski, *A scalable realization of local $u(1)$ gauge invariance in cold atomic mixtures*, Science **367**(6482), 1128 (2020), doi:[10.1126/science.aaz5312](https://doi.org/10.1126/science.aaz5312), <https://www.science.org/doi/pdf/10.1126/science.aaz5312>.
- [22] B. Yang, H. Sun, R. Ott, H.-Y. Wang, T. V. Zache, J. C. Halimeh, Z.-S. Yuan, P. Hauke and J.-W. Pan, *Observation of gauge invariance in a 71-site bose–hubbard quantum simulator*, Nature **587**(7834), 392–396 (2020), doi:[10.1038/s41586-020-2910-8](https://doi.org/10.1038/s41586-020-2910-8).
- [23] R. C. Brower, D. Berenstein and H. Kawai, *Lattice gauge theory for a quantum computer* (2020), <http://arXiv.org/abs/2002.10028>.
- [24] S. Choi, C. J. Turner, H. Pichler, W. W. Ho, A. A. Michailidis, Z. Papić, M. Serbyn, M. D. Lukin and D. A. Abanin, *Emergent $su(2)$ dynamics and perfect quantum many-body scars*, Phys. Rev. Lett. **122**, 220603 (2019), doi:[10.1103/PhysRevLett.122.220603](https://doi.org/10.1103/PhysRevLett.122.220603).

- [25] W. W. Ho, S. Choi, H. Pichler and M. D. Lukin, *Periodic orbits, entanglement, and quantum many-body scars in constrained models: Matrix product state approach*, Phys. Rev. Lett. **122**, 040603 (2019), doi:[10.1103/PhysRevLett.122.040603](https://doi.org/10.1103/PhysRevLett.122.040603).
- [26] C.-J. Lin and O. I. Motrunich, *Exact quantum many-body scar states in the rydberg-blockaded atom chain*, Phys. Rev. Lett. **122**, 173401 (2019), doi:[10.1103/PhysRevLett.122.173401](https://doi.org/10.1103/PhysRevLett.122.173401).
- [27] T. Iadecola, M. Schechter and S. Xu, *Quantum many-body scars from magnon condensation*, Phys. Rev. B **100**, 184312 (2019), doi:[10.1103/PhysRevB.100.184312](https://doi.org/10.1103/PhysRevB.100.184312).
- [28] N. Shiraishi, *Connection between quantum-many-body scars and the afleck-kennedy-lieb-tasaki model from the viewpoint of embedded hamiltonians*, Journal of Statistical Mechanics: Theory and Experiment **2019**(8), 083103 (2019), doi:[10.1088/1742-5468/ab342e](https://doi.org/10.1088/1742-5468/ab342e).
- [29] S. Chattopadhyay, H. Pichler, M. D. Lukin and W. W. Ho, *Quantum many-body scars from virtual entangled pairs*, Phys. Rev. B **101**, 174308 (2020), doi:[10.1103/PhysRevB.101.174308](https://doi.org/10.1103/PhysRevB.101.174308).
- [30] B. Mukherjee, S. Nandy, A. Sen, D. Sen and K. Sengupta, *Collapse and revival of quantum many-body scars via floquet engineering*, Phys. Rev. B **101**, 245107 (2020), doi:[10.1103/PhysRevB.101.245107](https://doi.org/10.1103/PhysRevB.101.245107).
- [31] B. Mukherjee, Z. Cai and W. V. Liu, *Constraint-induced breaking and restoration of ergodicity in spin-1 pxp models*, Phys. Rev. Research **3**, 033201 (2021), doi:[10.1103/PhysRevResearch.3.033201](https://doi.org/10.1103/PhysRevResearch.3.033201).
- [32] S. Pai and M. Pretko, *Dynamical scar states in driven fracton systems*, Phys. Rev. Lett. **123**, 136401 (2019), doi:[10.1103/PhysRevLett.123.136401](https://doi.org/10.1103/PhysRevLett.123.136401).
- [33] B. Mukherjee, A. Sen, D. Sen and K. Sengupta, *Dynamics of the vacuum state in a periodically driven rydberg chain*, Phys. Rev. B **102**, 075123 (2020), doi:[10.1103/PhysRevB.102.075123](https://doi.org/10.1103/PhysRevB.102.075123).
- [34] B. Mukherjee, A. Sen, D. Sen and K. Sengupta, *Restoring coherence via aperiodic drives in a many-body quantum system*, Phys. Rev. B **102**, 014301 (2020), doi:[10.1103/PhysRevB.102.014301](https://doi.org/10.1103/PhysRevB.102.014301).
- [35] K. Mizuta, K. Takasan and N. Kawakami, *Exact floquet quantum many-body scars under rydberg blockade*, Phys. Rev. Research **2**, 033284 (2020), doi:[10.1103/PhysRevResearch.2.033284](https://doi.org/10.1103/PhysRevResearch.2.033284).
- [36] A. A. Michailidis, C. J. Turner, Z. Papić, D. A. Abanin and M. Serbyn, *Stabilizing two-dimensional quantum scars by deformation and synchronization*, Phys. Rev. Research **2**, 022065 (2020), doi:[10.1103/PhysRevResearch.2.022065](https://doi.org/10.1103/PhysRevResearch.2.022065).
- [37] C.-J. Lin, V. Calvera and T. H. Hsieh, *Quantum many-body scar states in two-dimensional rydberg atom arrays*, Phys. Rev. B **101**, 220304 (2020), doi:[10.1103/PhysRevB.101.220304](https://doi.org/10.1103/PhysRevB.101.220304).
- [38] F. M. Surace, P. P. Mazza, G. Giudici, A. Lerose, A. Gambassi and M. Dalmonte, *Lattice gauge theories and string dynamics in rydberg atom quantum simulators*, Physical Review X **10**(2) (2020), doi:[10.1103/physrevx.10.021041](https://doi.org/10.1103/physrevx.10.021041).

- [39] D. Banerjee and A. Sen, *Quantum scars from zero modes in an abelian lattice gauge theory on ladders*, Phys. Rev. Lett. **126**, 220601 (2021), doi:[10.1103/PhysRevLett.126.220601](https://doi.org/10.1103/PhysRevLett.126.220601).
- [40] S. Biswas, D. Banerjee and A. Sen, *Scars from protected zero modes and beyond in $U(1)$ quantum link and quantum dimer models*, SciPost Phys. **12**, 148 (2022), doi:[10.21468/SciPostPhys.12.5.148](https://doi.org/10.21468/SciPostPhys.12.5.148).
- [41] J. Wildeboer, A. Seidel, N. S. Srivatsa, A. E. B. Nielsen and O. Erten, *Topological quantum many-body scars in quantum dimer models on the kagome lattice*, Phys. Rev. B **104**, L121103 (2021), doi:[10.1103/PhysRevB.104.L121103](https://doi.org/10.1103/PhysRevB.104.L121103).
- [42] B. Mukherjee, A. Sen and K. Sengupta, *Periodically driven rydberg chains with staggered detuning*, Phys. Rev. B **106**, 064305 (2022), doi:[10.1103/PhysRevB.106.064305](https://doi.org/10.1103/PhysRevB.106.064305).
- [43] J.-Y. Desaulles, D. Banerjee, A. Hudomal, Z. Papić, A. Sen and J. C. Halimeh, *Weak ergodicity breaking in the schwinger model*, doi:[10.48550/ARXIV.2203.08830](https://doi.org/10.48550/ARXIV.2203.08830) (2022).
- [44] J.-Y. Desaulles, A. Hudomal, D. Banerjee, A. Sen, Z. Papić and J. C. Halimeh, *Prominent quantum many-body scars in a truncated schwinger model* (2022), [2204.01745](https://arxiv.org/abs/2204.01745).
- [45] A. Hudomal, J.-Y. Desaulles, B. Mukherjee, G.-X. Su, J. C. Halimeh and Z. Papić, *Driving quantum many-body scars*, doi:[10.48550/ARXIV.2204.13718](https://doi.org/10.48550/ARXIV.2204.13718) (2022).
- [46] A. Smith, J. Knolle, D. L. Kovrizhin and R. Moessner, *Disorder-free localization*, Phys. Rev. Lett. **118**, 266601 (2017), doi:[10.1103/PhysRevLett.118.266601](https://doi.org/10.1103/PhysRevLett.118.266601).
- [47] P. Karpov, R. Verdel, Y.-P. Huang, M. Schmitt and M. Heyl, *Disorder-free localization in an interacting 2d lattice gauge theory*, Phys. Rev. Lett. **126**, 130401 (2021), doi:[10.1103/PhysRevLett.126.130401](https://doi.org/10.1103/PhysRevLett.126.130401).
- [48] N. Chakraborty, M. Heyl, P. Karpov and R. Moessner, *Disorder-free localization transition in a two-dimensional lattice gauge theory*, doi:[10.48550/ARXIV.2203.06198](https://doi.org/10.48550/ARXIV.2203.06198) (2022).
- [49] M. Brenes, M. Dalmonte, M. Heyl and A. Scardicchio, *Many-body localization dynamics from gauge invariance*, Phys. Rev. Lett. **120**, 030601 (2018), doi:[10.1103/PhysRevLett.120.030601](https://doi.org/10.1103/PhysRevLett.120.030601).
- [50] P. Sala, T. Rakovszky, R. Verresen, M. Knap and F. Pollmann, *Ergodicity breaking arising from hilbert space fragmentation in dipole-conserving hamiltonians*, Phys. Rev. X **10**, 011047 (2020), doi:[10.1103/PhysRevX.10.011047](https://doi.org/10.1103/PhysRevX.10.011047).
- [51] V. Khemani, M. Hermele and R. Nandkishore, *Localization from hilbert space shattering: From theory to physical realizations*, Phys. Rev. B **101**, 174204 (2020), doi:[10.1103/PhysRevB.101.174204](https://doi.org/10.1103/PhysRevB.101.174204).
- [52] A. Pal and D. A. Huse, *Many-body localization phase transition*, Phys. Rev. B **82**, 174411 (2010), doi:[10.1103/PhysRevB.82.174411](https://doi.org/10.1103/PhysRevB.82.174411).
- [53] R. Nandkishore and D. A. Huse, *Many-body localization and thermalization in quantum statistical mechanics*, Annual Review of Condensed Matter Physics **6**(1), 15 (2015), doi:[10.1146/annurev-conmatphys-031214-014726](https://doi.org/10.1146/annurev-conmatphys-031214-014726), <https://doi.org/10.1146/annurev-conmatphys-031214-014726>.

- [54] D. A. Abanin, E. Altman, I. Bloch and M. Serbyn, *Colloquium: Many-body localization, thermalization, and entanglement*, Rev. Mod. Phys. **91**, 021001 (2019), doi:[10.1103/RevModPhys.91.021001](https://doi.org/10.1103/RevModPhys.91.021001).
- [55] S. Moudgalya, A. Prem, R. Nandkishore, N. Regnault and B. A. Bernevig, *Thermalization and Its Absence within Krylov Subspaces of a Constrained Hamiltonian*, chap. Chapter 7, pp. 147–209, doi:[10.1142/9789811231711_0009](https://doi.org/10.1142/9789811231711_0009), https://www.worldscientific.com/doi/pdf/10.1142/9789811231711_0009.
- [56] S. Pai, M. Pretko and R. M. Nandkishore, *Localization in fractonic random circuits*, Phys. Rev. X **9**, 021003 (2019), doi:[10.1103/PhysRevX.9.021003](https://doi.org/10.1103/PhysRevX.9.021003).
- [57] Z.-C. Yang, F. Liu, A. V. Gorshkov and T. Iadecola, *Hilbert-space fragmentation from strict confinement*, Phys. Rev. Lett. **124**, 207602 (2020), doi:[10.1103/PhysRevLett.124.207602](https://doi.org/10.1103/PhysRevLett.124.207602).
- [58] T. Rakovszky, P. Sala, R. Verresen, M. Knap and F. Pollmann, *Statistical localization: From strong fragmentation to strong edge modes*, Phys. Rev. B **101**, 125126 (2020), doi:[10.1103/PhysRevB.101.125126](https://doi.org/10.1103/PhysRevB.101.125126).
- [59] J. Feldmeier, P. Sala, G. De Tomasi, F. Pollmann and M. Knap, *Anomalous diffusion in dipole- and higher-moment-conserving systems*, Phys. Rev. Lett. **125**, 245303 (2020), doi:[10.1103/PhysRevLett.125.245303](https://doi.org/10.1103/PhysRevLett.125.245303).
- [60] P. A. McClarty, M. Haque, A. Sen and J. Richter, *Disorder-free localization and many-body quantum scars from magnetic frustration*, Phys. Rev. B **102**, 224303 (2020), doi:[10.1103/PhysRevB.102.224303](https://doi.org/10.1103/PhysRevB.102.224303).
- [61] L. Herviou, J. H. Bardarson and N. Regnault, *Many-body localization in a fragmented hilbert space*, Phys. Rev. B **103**, 134207 (2021), doi:[10.1103/PhysRevB.103.134207](https://doi.org/10.1103/PhysRevB.103.134207).
- [62] K. Lee, A. Pal and H. J. Changlani, *Frustration-induced emergent hilbert space fragmentation*, Phys. Rev. B **103**, 235133 (2021), doi:[10.1103/PhysRevB.103.235133](https://doi.org/10.1103/PhysRevB.103.235133).
- [63] S. Roy and A. Lazarides, *Strong ergodicity breaking due to local constraints in a quantum system*, Phys. Rev. Research **2**, 023159 (2020), doi:[10.1103/PhysRevResearch.2.023159](https://doi.org/10.1103/PhysRevResearch.2.023159).
- [64] B. Mukherjee, D. Banerjee, K. Sengupta and A. Sen, *Minimal model for hilbert space fragmentation with local constraints*, Phys. Rev. B **104**, 155117 (2021), doi:[10.1103/PhysRevB.104.155117](https://doi.org/10.1103/PhysRevB.104.155117).
- [65] B. Pozsgay, T. Gombor, A. Hutsalyuk, Y. Jiang, L. Pristyák and E. Vernier, *Integrable spin chain with hilbert space fragmentation and solvable real-time dynamics*, Phys. Rev. E **104**, 044106 (2021), doi:[10.1103/PhysRevE.104.044106](https://doi.org/10.1103/PhysRevE.104.044106).
- [66] C. M. Langlett and S. Xu, *Hilbert space fragmentation and exact scars of generalized fredkin spin chains*, Phys. Rev. B **103**, L220304 (2021), doi:[10.1103/PhysRevB.103.L220304](https://doi.org/10.1103/PhysRevB.103.L220304).
- [67] D. Hahn, P. A. McClarty and D. J. Luitz, *Information Dynamics in a Model with Hilbert Space Fragmentation*, SciPost Phys. **11**, 74 (2021), doi:[10.21468/SciPostPhys.11.4.074](https://doi.org/10.21468/SciPostPhys.11.4.074).
- [68] A. Khudorozhkov, A. Tiwari, C. Chamon and T. Neupert, *Hilbert space fragmentation in a 2d quantum spin system with subsystem symmetries*, doi:[10.48550/ARXIV.2107.09690](https://doi.org/10.48550/ARXIV.2107.09690) (2021).

- [69] S. Moudgalya, B. A. Bernevig and N. Regnault, *Quantum many-body scars and hilbert space fragmentation: A review of exact results*, doi:[10.48550/ARXIV.2109.00548](https://doi.org/10.48550/ARXIV.2109.00548) (2021).
- [70] A. Paramekanti, L. Balents and M. P. A. Fisher, *Ring exchange, the exciton bose liquid, and bosonization in two dimensions*, Phys. Rev. B **66**, 054526 (2002), doi:[10.1103/PhysRevB.66.054526](https://doi.org/10.1103/PhysRevB.66.054526).
- [71] A. W. Sandvik, S. Daul, R. R. P. Singh and D. J. Scalapino, *Striped phase in a quantum xy model with ring exchange*, Phys. Rev. Lett. **89**, 247201 (2002), doi:[10.1103/PhysRevLett.89.247201](https://doi.org/10.1103/PhysRevLett.89.247201).
- [72] R. G. Melko, A. W. Sandvik and D. J. Scalapino, *Two-dimensional quantum XY model with ring exchange and external field*, Phys. Rev. B **69**, 100408 (2004), doi:[10.1103/PhysRevB.69.100408](https://doi.org/10.1103/PhysRevB.69.100408).
- [73] M. Schecter and T. Iadecola, *Many-body spectral reflection symmetry and protected infinite-temperature degeneracy*, Phys. Rev. B **98**, 035139 (2018), doi:[10.1103/PhysRevB.98.035139](https://doi.org/10.1103/PhysRevB.98.035139).
- [74] R. J. Baxter, *Planar lattice gases with nearest-neighbor exclusion*, Annals of Combinatorics **3**(2), 191 (1999), doi:[10.1007/BF01608783](https://doi.org/10.1007/BF01608783).
- [75] M. Medenjak, B. Buča and D. Jaksch, *Isolated heisenberg magnet as a quantum time crystal*, Phys. Rev. B **102**, 041117 (2020), doi:[10.1103/PhysRevB.102.041117](https://doi.org/10.1103/PhysRevB.102.041117).
- [76] V. Oganesyan and D. A. Huse, *Localization of interacting fermions at high temperature*, Phys. Rev. B **75**, 155111 (2007), doi:[10.1103/PhysRevB.75.155111](https://doi.org/10.1103/PhysRevB.75.155111).
- [77] Y. Y. Atas, E. Bogomolny, O. Giraud and G. Roux, *Distribution of the ratio of consecutive level spacings in random matrix ensembles*, Phys. Rev. Lett. **110**, 084101 (2013), doi:[10.1103/PhysRevLett.110.084101](https://doi.org/10.1103/PhysRevLett.110.084101).
- [78] W. Buijsman, *Number of zero-energy eigenstates in the pxp model*, doi:[10.48550/ARXIV.2203.09264](https://doi.org/10.48550/ARXIV.2203.09264) (2022).
- [79] K. Bull, J.-Y. Desaules and Z. Papić, *Quantum scars as embeddings of weakly broken lie algebra representations*, Phys. Rev. B **101**, 165139 (2020), doi:[10.1103/PhysRevB.101.165139](https://doi.org/10.1103/PhysRevB.101.165139).
- [80] J. Lehmann, P. Sala, F. Pollmann and T. Rakovszky, *Fragmentation-induced localization and boundary charges in dimensions two and above*, doi:[10.48550/ARXIV.2208.12260](https://doi.org/10.48550/ARXIV.2208.12260) (2022).